MSc thesis in Process & Energy

Assessing Lift and Drag in Front Crawl Swimming: the Straight or Curved Pull

Willis Houtman
2023

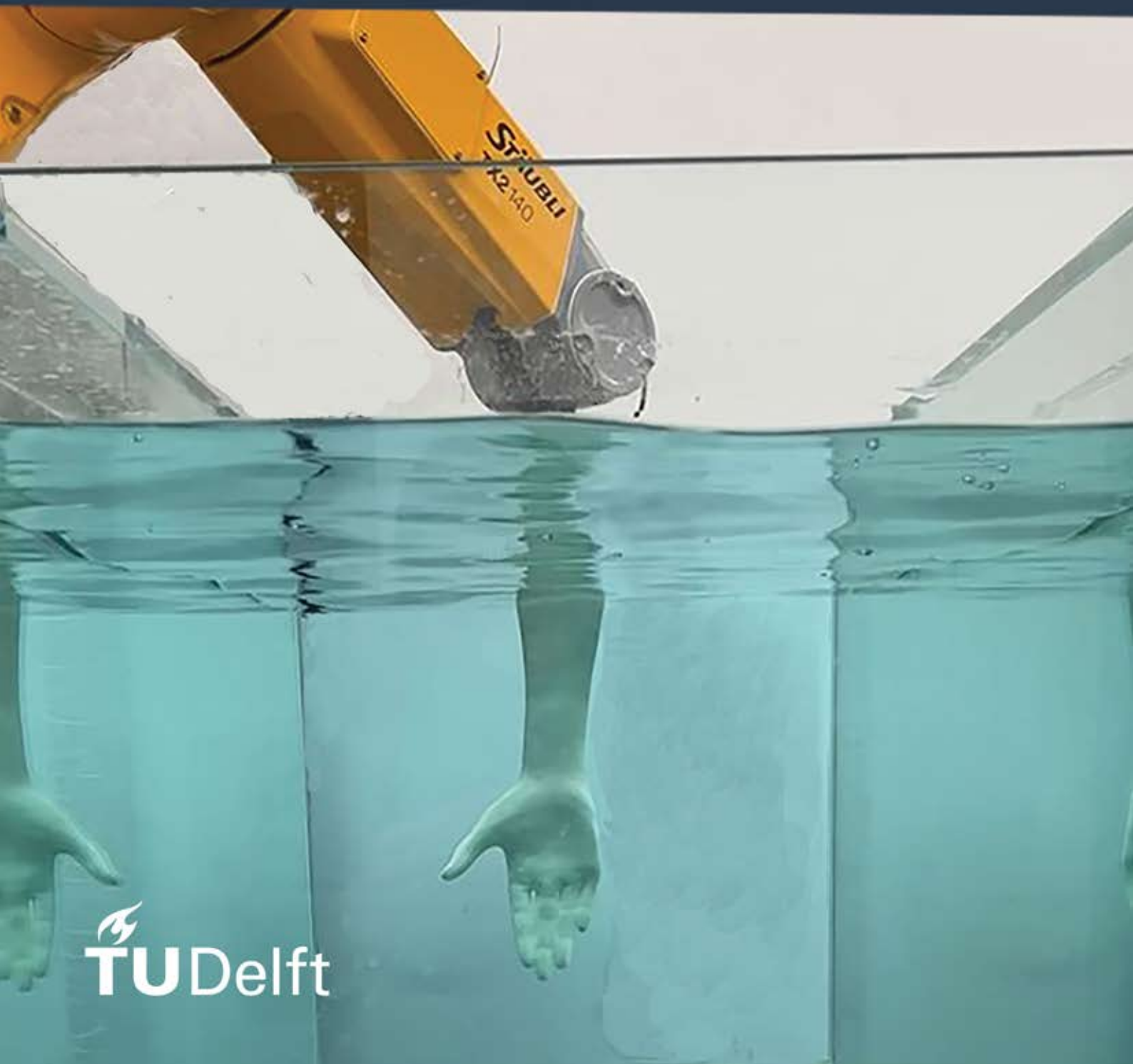

TU Delft

Assessing Lift and Drag in Front Crawl Swimming: the Straight or Curved Pull

Willis Houtman

A thesis submitted to the Delft University of Technology in partial fulfilment of the requirements for the degree of Master of Science, to be defended publicly on Tuesday September 26, 2023 at 03:00 PM.

Willis Houtman: *Assessing Lift and Drag in Front Crawl Swimming: the Straight or Curved Pull* (2023). An electronic version of this thesis can be found at http://repository.tudelft.nl.

The work in this thesis was carried out in the:

Fluid mechanics group
Process & Energy department of the faculty of Mechanical, Maritime and Materials Engineering
Delft University of Technology

Student number:	4450841	
Project duration	November 23, 2022 - September 26, 2023	
Thesis committee:	Prof.dr.ir. J. Westerweel,	TUDelft, supervisor
	ir. A. Greidanus,	TUDelft, supervisor
	Prof.dr.ir. W. van de Water,	TUDelft, supervisor
	G. Mulder,	TUDelft
	dr. P. Costa,	TUDelft

Abstract

Swimming is a sport where an incremental gain in performance can lead to either a medal or leaving the swimmer empty-handed. In the front crawl, water is driven backwards by the limbs, where most propulsive forces come from the hands. Two main stroke patterns can be observed, the ”straight I-pull” is commonly taught to generate forces with drag, and the ”curved S-pull” applies lift as well. This investigation uses a new industrial 6-DOF robot arm to study angle-dependent forces, stroke patterns and hand configuration variables. The forearm and hand are analysed using force measurements and PIV to obtain quantitative information, while a parameterisation of the forearm and hand is used to obtain qualitative analysis. The flow is analysed qualitatively using two analytical methods, but it is discovered that these methods can only be applied to a limited range of cases to predict the angle-dependent lift force. Numerical investigations into the parameterised arm model reveal that forces generated were similar in magnitude to those reported in the literature for a pseudo-transient simulation. Quantitative research shows that lift only surpasses drag at extreme angles of attack immediately after a rapid start. This provides clear evidence that drag-based propulsion is preferred for front-crawl swimming. We utilize PIV technology to visualise the flow field around two cases where the lift was highly prevalent. The results reveal various aspects, including the nature of the observed lift peak. Finally, the study compares three distinct strokes: one utilizing a straight drag-based approach and two utilizing a sinusoidal path, resembling a curved pull. The findings indicate that the sinusoidal path’s lift-to-drag ratio remains relatively consistent compared to steady-state, constant-angle experiments. Additionally, the results suggest that the straight stroke is optimal for propulsion, while one of the sinusoidal strokes might be more energy-efficient. An additional aim of this research is to determine the suitability of an industrial 6-DOF robot arm for stroke experiments. It is discovered that some experiments need a longer path and should preferably be conducted in a wind or water tunnel.

Acknowledgements

This thesis report marks the end of my two-year's master degree studying Energy & Process. In the last nine months, I have been working on various aspects surrounding the force generation in swimming; during this time many people have helped and guided and I would like to take the opportunity to thank them.
First, I want to thank GertJan Mulder for all the hours working on the robot arm and facilitating my experiments, that you were always approachable and for your never-ending humour and enthusiasm. Furthermore, I would like to thank prof. dr. ir. Willem de Water for his insights and help on this thesis's theoretical aspects. I would also like to thank prof. dr. ir. Jerry Westerweel, for his overall knowledge and valuable insights in the topic of swimming. Likewise, I want to thank Prof. dr. Arnoud Greidanus for his insights into the experimental work of this thesis.
I would also sincerely like to thank ir. Edwin Overmars, for his help setting up the PIV; even though, due to the renovation, there wasn't a lot of time, you still helped me greatly. I want to thank dr. ir. Mathieu Pourquie for his help on the CFD simulations. Furthermore, I would like to thank dr. Pedro Costa for making the time and effort to take part as the external member in my thesis committee.

Contents

List of Figures

Nomenclature

Physical Constants

g	Gravitational acceleration	$9\,81\mathrm{m/s^2}$

Greek Symbols

α	Angle of attack	$\circ$
β	Eccentricity	–
$\dot{\alpha}$	angular velocity of the angle of attack	s^{-1}
ϵ	Blockage factor	–
η_i	Starting angle ellipse	$\circ$
η_E	Energetic efficiency	$\mathrm{s\,m}^{-1}$
η_F	Froude efficiency	–
η_J	Impulse efficiency	–
Γ	Circulation	$\mathrm{m}^2\,\mathrm{s}^{-1}$
γ	Sweepback angle	$\circ$
ν	Kinematic viscosity	$\mathrm{m}^2\,\mathrm{s}^{-1}$
ϕ	Blockage ratio	–
ϕ	Velocity potential	$\mathrm{m}^2\,\mathrm{s}^{-1}$
ψ	Stream function	$\mathrm{kg\,m}^{-1}\,\mathrm{s}$
ρ	Density	$\mathrm{kg\,m}^{-3}$
ρ_f	Particle density	$\mathrm{kg\,m}^{-3}$
ρ_p	Fluid density	$\mathrm{kg\,m}^{-3}$
τ_f	Characteristic time scale of a object	s
τ_p	Characteristic time scale of a particle	s
θ	Pitch angle	$\circ$

ξ	Variable related to eccentricity	–
ζ	Complex variable	–
f	Shedding frequency	Hz

Other Symbols

$\mathbf{J}$	Impulse vector	$\mathrm{kg\,m\,s^{-1}}$
a	Acceleration	$\mathrm{m\,s^{-2}}$
a_1	Semi-major axis	m
a_2	Semi-minor axis	m
A_p	Projected area	$\mathrm{m^2}$
C_{add}	Added mass coefficient	–
C_D	Drag coefficient	–
C_L	Lift coefficient	–
$C_{D,c}$	Corrected Drag coefficient	–
$C_{L,c}$	Corrected Lift coefficient	–
d_p	Particle diameter	m
E	Total spent energy	$\mathrm{kg\,m^2\,s^{-2}}$
F_D	Drag force	N
F'_L	Lift per unit span	$\mathrm{N\,m^{-1}}$
F_L	Lift force	N
L_h	Characteristic length scale of the hand	m
m_{add}	Added mass	kg
P	Instantaneous power	$\mathrm{kg\,m^2\,s^{-3}}$
r	Radius	m
U	Velocity	$\mathrm{m\,s^{-1}}$
u	Velocity in x-direction	$\mathrm{m\,s^{-1}}$
u_τ	Friction velocity	$\mathrm{m\,s^{-1}}$
V	Volume	$\mathrm{m^3}$

v	Velocity in y-direction	$\mathrm{m\,s^{-1}}$
v_{ref}	Characteristic velocity scale	$\mathrm{m\,s^{-1}}$
z	Complex variable in conformal map domain	–

Dimensionless numbers

Fr	Froude number	–
Re	Reynolds number	–
St	Strouhal number	–
St_p	Stokes number	–
$y+$	Wall y+	

1. Introduction

Swimming is a sport where even the slightest improvement in technique can significantly affect results. Highlighting one example of many, in the 2020 Olympic freestyle men's final of 200 meters, the time difference between first and seventh place was less than one percent. This shows how crucial even the smallest improvement in technique can be in determining whether a swimmer will win an Olympic medal or leave the competition empty-handed. Connecting the fundamental principles of fluid mechanics with this sport to enhance performance and gain a deeper comprehension of swimming is crucial. There is a debate in the field regarding the superiority of using a "straight I-pull" or a "curved S-pull." Various propulsive forces come into play, and this thesis aims to examine these forces thoroughly.

Previous research has examined various factors that affect swimming performance. In this thesis, we aim to investigate the effects of finger spreading and stroke movements on swimming performance, both in steady and unsteady conditions. To conduct experiments, we will be using a new six DOF Stäubli industrial robot arm; the initial stage will involve testing the arm.

This thesis starts by delving into previous investigations and concepts related to front crawl swimming. Firstly, general information about front crawl swimming is provided, followed by an explanation of relevant drag and lift concepts. The third section explores how drag and lift relate to front crawl swimming. Finally, the chapter will conclude with a discussion on scaling and the blockage effect before presenting the research objectives and the outline of this thesis research.

1.1 Front Crawl Swimming

The front crawl stroke is the quickest swimming technique among the four main strokes. It is used in freestyle and is commonly referred to as such. Along with the backstroke, it involves reciprocal limb movements that are not synchronised, unlike the butterfly and breaststroke.

The arm movement in front crawl swimming can be divided into five recognisable stages. The entry and catch phase occurs when the arm enters and catches the water and ends when the arm begins its backward movement. The pull phase follows, during which the arm starts its backwards motion and starts generating propulsive forces. It ends when the arm is in the vertical plane of the shoulder. The generation of maximal propulsive forces characterises the push phase and ends when the hand releases the water. Finally, the recovery phase occurs when the hand is out of the water, and the arm is recovering for the next stroke (Chollet et al. [2000]).

Another way to characterise the swimming stroke is in terms of the downsweep, the insweep and the upsweep, as seen in Figure 1.2a. Here the downsweep is the backward movement of the hand to the outermost y-coordinate, the insweep is the movement of the hand with a changed velocity vector towards the centerline of the body ending when the arm reaches the maximum z-coordinate and the upsweep where the motion changes direction towards the outward and upward direction (Takagi et al. [2014a]).

The hand orientation in swimming is defined in terms of the angle of attack, α, which

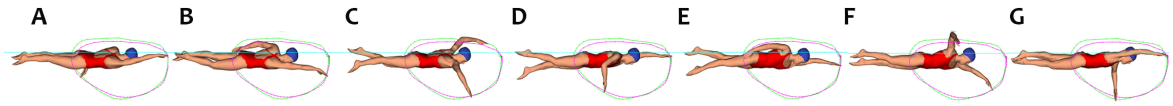

Figure 1.1.: Front crawl swimming stroke phases, for the right arm; **A**) the end of the entry and catch phase, **B**) beginning of the pull phase, **C**) end of the pull phase, **D**) beginning of the push phase, where the arm is in the vertical plane of the shoulder, **E**) start of the recovery phase, where the arm is out of the water, **F**) start of the entry and catch phase and **G**), the start of the new stroke, edited from Cohen et al. [2017].

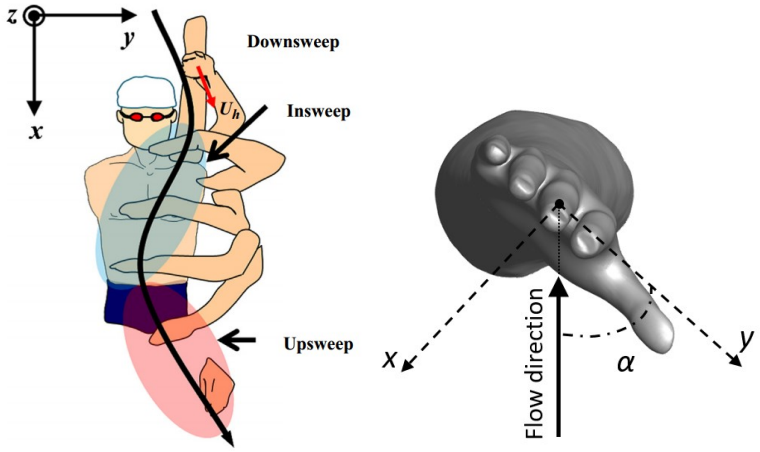

Figure 1.2.: (a) Characterisation of a front crawl arm stroke in three phases; the *downsweep*, where the arm starts its backward movement until the maximum value of the y-coordinate has been reached, the *insweep*, where the direction of movement is changed towards the centerline, ending at the maximum value for the z-coordinate and the *upsweep*, where the arm moves outwards and upwards, from Takagi et al. [2014a]. (b) Definition of attack angle α, which is the angle between the thumb (y-axis) and the flow direction

is the angle between the y-axis and the flow direction. The definition used in this thesis can be seen schematically in Figure 1.2b. The other angles commonly used are the pitch angle, θ, which is the angle between the hand plane and the flow direction and the sweepback angle, γ, which is the angle between the flow direction and the arm, perpendicular to the hand plane.

1.2 Drag and lift mechanisms

The force that resists a body moving through a medium is called drag. It is always directed opposite to the object's motion, while the lift is the force perpendicular to the object's movement. Drag and lift forces are defined by,

$$F_{D,L} = \frac{1}{2}\rho A_p U^2 C_{D,L}, \tag{1.1}$$

where ρ is the density of the fluid, A_p is the projected surface perpendicular to the flow, U is the velocity, and $C_{D,L}$ is the specific dimensionless drag or lift coefficient for the object (van Houwelingen et al. [2017a]). The drag and lift coefficients generally depend on the object's shape and the Reynolds number, which is a dimensionless number representing the ratio of inertial and viscous forces. The Reynolds number is defined as,

$$\mathrm{Re} = \frac{UL_{ref}}{\nu}, \tag{1.2}$$

with U the flow velocity, L_{ref} the characteristic length of the object and ν the kinematic viscosity of the fluid. The Reynolds number is also used for scaling to express dynamic similarity between experiments and/or simulations (White [2011]). At the critical Reynolds number, the flow transitions from laminar to turbulent and at high Reynolds numbers, inertia forces dominate, the subsequent drag force generally scales with U^2 (Kundu et al. [2016]).
Equation 1.1 only considers the force coefficients at a steady-state fluid flow. Acceleration of a body in water increases the kinetic energy of the surrounding flow, requiring additional work by the body, which can be considered as the added mass force (van Houwelingen et al. [2017a]). This force is added to equation 1.1, leading to the time-dependent drag force equation (Sarpkaya [1986]),

$$F(t) = am_{\text{add}} + \frac{1}{2}A_p\rho U(t)^2 C_D(U(t)), \tag{1.3}$$

where a is the acceleration, $C_D(U(t))$ the velocity-dependent drag coefficient, and the added mass, $m_{\text{add}} = C_{\text{add}}\rho V$, with V being the volume of the body and C_{add} a constant relating the added mass to the total mass of the object (Brennen [1982]; van Houwelingen et al. [2017a]). The total hydrodynamic drag on a body moving through water consists of three types of drag; viscous, pressure and wave drag (Marinho et al. [2011]). At different velocities, different drag mechanisms are dominant. These will be described in the coming paragraphs.

1.2.1 Viscous drag

Viscous or skin friction drag originates from fluid viscosity, and it produces shear stresses in the boundary layer, defined as the layer where the mean streamwise velocity increases from zero at the surface to 99 % of the free stream value (Truijens and Toussaint [2005]; Marinho et al. [2011]). The magnitude of viscous drag depends on the total wetted area and the flow conditions in the boundary layer. Depending on the Reynolds number, the flow in the boundary layer can be laminar or turbulent.

1.2.2 Pressure drag

Pressure drag dominates flows around blunt bodies e.g. a cylinder perpendicular to the flow, where wakes are formed due to flow separation outside the boundary layer. In the wake, where the flow is separated, the flow reverses and rolls up into eddies (vortices) depending on the shape of the object (Kundu et al. [2016]). The vortices generate a pressure differential over the object, resulting in pressure drag.

Circular cylinders

For circular cylinders, a sudden decrease of the drag coefficient is observed between $3 \cdot 10^5 < \mathrm{Re} < 3 \cdot 10^6$, the boundary layer transitions from laminar (with a broad wake) to turbulent with a narrower wake (Kundu et al. [2016]). For laminar separation, the pressure in the wake of the separation point is constant and lower than the upstream pressure; this pressure differential leads to an approximately constant drag coefficient over a wide range as the separation point of 82° does not change. For the turbulent wake, the separation point is

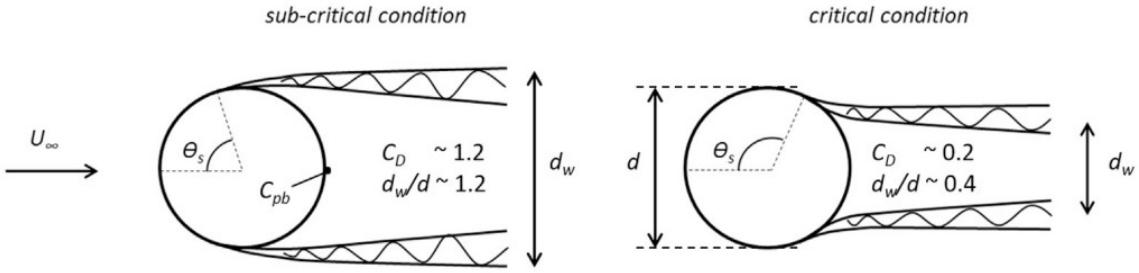

Figure 1.3.: Image showing the flow around a circular cylinder in two different conditions - sub-critical on the left and critical on the right. When the wake around the cylinder changes from laminar to turbulent, there is a sudden decrease in the drag coefficient, known as the drag crisis, from Terra et al. [2020].

at 125°, leading to a narrower wake and a smaller pressure differential. Both contribute to a sudden drop in the drag coefficient.

1.2.3 Wave drag

Moving near the water's surface creates an additional force of resistance on the body known as wave drag. As the object pierces through the free water surface, generated kinetic energy from the object is lost and changed into energy in the formation of waves (Kundu et al. [2016]). The need to overcome the wave reduces the object's ability to increase speed. The Froude number (Fr) is a dimensionless number that quantifies the similarity of free-surface flows and compares the object's ability to overcome wave drag. It is defined as,

$$\mathrm{Fr} = \frac{U}{\sqrt{gL_{ref}}}, \tag{1.4}$$

where g is the gravitational acceleration. According to the research of Kudo et al. [2008], when the arm surface penetrates and creates wave drag, the drag coefficient value (C_D) goes up significantly, by as much as $46 - 98\,\%$. However, this effect has a lesser impact on the lift coefficient (C_L), with reported values of $2 - 12\,\%$. .

1.2.4 Vorticity dynamics

In fluid mechanics, vorticity is the physical quantity characterising the rotation of fluid elements. It is a vector amounting to two times the angular velocity of a fluid parcel and is useful for describing and understanding various interesting phenomena.

$$\boldsymbol{\omega} = \nabla \times \mathbf{u}. \tag{1.5}$$

Hydrofoil

To illustrate the link between vorticity and lift, a hydrofoil is considered. A hydrofoil is a cross-section shape of a body that can generate lift and drag forces if placed in a fluid's motion. A human hand undergoing front crawl propulsion resembles a hydrofoil with a large angle of attack. Figure 1.4 shows the terminology of a standard hydrofoil. The hydrofoil is composed of a leading edge, where the incoming fluid is divided, and a trailing edge, where the split flows combine. The asymmetrical positioning of these stagnation points results in

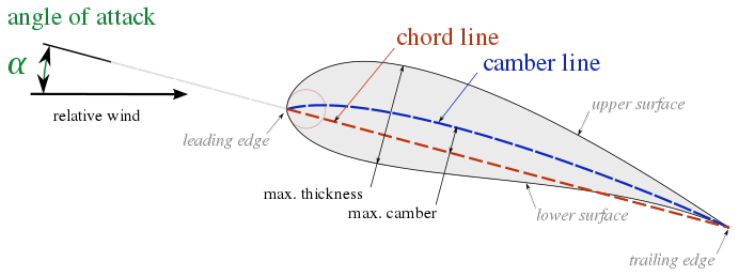

Figure 1.4.: Nomenclature hydrofoil, from Mahasidha R. Birajdar [2015].

a velocity differential in the flow, with greater velocities around the top compared to the bottom. Applying Bernoulli's principle, this velocity difference creates a pressure difference, resulting in lift. As a body moves through the water, it generates forces while creating a wake; these two efforts are interrelated as the forces acting on a body must be countered by an equal and opposite change in the fluid momentum.

In fluid mechanics, the circulation Γ is the integrated vorticity (Kundu et al. [2016]). Stokes' theorem relates it to the line integral of the velocity over a closed contour that bounds A,

$$\Gamma = \oint_C \mathbf{u} \cdot dl = \iint_A \boldsymbol{\omega} \cdot \boldsymbol{n} \, dA, \tag{1.6}$$

where dl is the line increment tangent to the curve, A is the surface that caps the curve, and $\mathbf{n}$ is the vector normal to the surface A.

The velocity differential around the top and bottom of a hydrofoil can also be expressed as a net circulation around the profile, the bound vortex. The relation between the circulation and the lift force can be expressed by the Kutta-Joukowski equation,

$$F'_L = \rho U \Gamma, \tag{1.7}$$

where F'_L is the lift per unit span, the total lift force F_L will equal $\rho U \Gamma$ integrated over the whole wing span. Combining equation 1.1 and 1.7 results in a relationship between the lift coefficient and the circulation,

$$C_L = \frac{2\Gamma}{U A_p}. \tag{1.8}$$

Kelvin's theorem is a fundamental conservation law in fluid mechanics and states that the net circulation in an inviscid, barotropic flow with conservative body forces cannot change. It can be expressed mathematically as,

$$D\boldsymbol{\Gamma}/Dt = 0. \tag{1.9}$$

This means that each motion-induced circulation is accompanied by an equal and opposite circulation close by (Dickinson [1996]). When initiating movement, the opposite circulation is expressed as a vortex forming near the starting point known as the starting vortex. To satisfy Kelvin's theorem, all the bound circulation is shed as a stopping vortex at the end of a motion,

precisely equal and opposite to the starting vortex.

In steady-state conditions, the bound circulation along a hydrofoil is time-invariant. However, in most forms of animal locomotion, including human swimming, conditions such as the angle of attack, velocity, and acceleration change throughout the stroke. As a result, the bound circulation is likely to change, causing non-steady force production and a more complex wake structure behind the hydrofoil (Dickinson [1996]).

Unsteady phenomenon

In the article by Dickinson [1996], various unsteady mechanisms of force generation are discussed, some of which are also relevant to swimming motion. The starting vortex formed due to Kelvin's theorem is opposite to the bound vortex along the hydrofoil. At steady state conditions, the starting vortex is so far away from the object that it hardly influences the flow over the object. In unsteady conditions, however, it does affect the circulatory lift at the onset of motion, as here, the starting vortex is still close-by. The starting vortex is opposite to the bound vortex, so they reduce each other's strength. This reduction is called the *Wagner effect* ([Dickinson, 1996]). According to Truijens and Toussaint [2005], the circulation takes up to six chord lengths to reach 90 % of its final value.

A second unsteady phenomenon arises when a hydrofoil has a large angle of attack (just like a human swimming hand). At an impulsive start, above a critical angle of attack, the flow separates at the leading edge, increasing the pressure drag and circulatory lift. This is called stall. An attached vortex is created and shed from the leading edge. It will reattach itself to the upper surface in front of the trailing edge, forming a leading edge bubble; as the leading edge grows, a small trailing edge vortex is developed to satisfy Kelvin's law. As the leading edge extends, von Kármán shedding will eventually occur. Because the separation does not happen instantaneously, it is also called dynamic or delayed stall (Dickinson [1996]). Due to the generated pressure differences, the attached vortices are strong and can generate sizeable propulsive lift forces. Figure 1.5 illustrates the dynamic or delayed stall process.

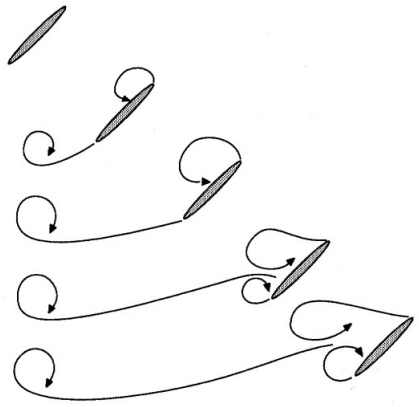

Figure 1.5.: Impulsive start of a small hydrofoil at a high angle of attack. The circulation does not stay bound to the hydrofoil but creates an attached vortex on the leading edge. As the attached leading edge vortex grows, an opposite trailing edge vortex is formed following Kelvin's theorem. Eventually, von Kármán shedding commences, from Dickinson [1996].

A staggered row of vortices shed behind a blunt body is called a von Kármán vortex street; due to the steady periodicity of the shedding at constant Reynolds number, the observed frequency Ω can be expressed as the dimensionless Strouhal number, $\mathrm{St} = fL/U$, where

the Strouhal number for a circular cylinder stays close to 0.2 for a wide range of Reynolds numbers (Kundu et al. [2016]). A jet flow can be observed between the two opposite shed vortices, which carry momentum and generate forward propulsion.

1.3 Drag and lift mechanisms in front crawl swimming

During swimming, a swimmer always has a gravitational force and an equal and opposite buoyancy force, a propulsive force and an opposite resistive force. The swimmer experiences two types of drag: hydrodynamic drag on the body, which should be minimised, and drag generated by the limbs, which results in forward propulsion, which should be maximised. If these two types of drag are equal, the swimmer will swim at a constant velocity. However, since the propulsive force fluctuates, the velocity is instationary.

The reciprocal motion of the limbs is the primary source of propulsive forces, and most of these forces come from the arm and hand (80-90 % according to Bilinauskaite et al. [2013] and van Houwelingen et al. [2017a]). Because the shape of the arm and hand are not streamlined, viscous drag is minimal, and pressure drag dominates (van Houwelingen et al. [2017a]). According to Cohen et al. [2017], the hand has a 2.5 times greater impact on drag compared to the arm. This is due to its larger frontal area and higher specific drag coefficient. Because of its significant influence on swimming performance, the hand is the most interesting to analyse in terms of improving performance. The propulsive force generated by the arms is mainly due to bluff body drag and can be compared to the flow around a cylinder.

Numerous studies have investigated the hydrodynamics of swimming, and the works of van Houwelingen et al. [2017a] and Wei et al. [2014] offer an extensive survey of the area. These reviews demonstrate that various factors affect propulsion, such as finger spacing, thumb position, hand orientation, kinematic parameters (e.g. acceleration and deceleration), and different stroke techniques (e.g. the S- and I-stroke).

Experiments and simulations on the hydrodynamics of the front crawl typically maintain a constant velocity, creating a quasi-steady state. However, research suggests that propulsive force increases under unsteady conditions, indicating the need for more realistic transient experiments or simulations (Rouboa et al. [2006]; Takagi et al. [2015]).

1.3.1 Unsteady experimentation

Most studies have focused on steady-state flow conditions, while in reality, the hand and arm experience varying rates of acceleration and deceleration during a swimming stroke. Pai and Hay [1988] first reported that the steady state approach greatly underestimated the propulsive forces when assessing movements involving high acceleration and deceleration. Several studies have shown that these unsteady flow conditions can result in significantly higher propulsive forces than steady-state flow conditions (e.g. Berger [1999]; Rouboa et al. [2006]; Kudo et al. [2013]; Bihan [2020]). However, no consensus exists on the underlying mechanisms responsible for these increased propulsive forces (Takagi et al. [2013]).

Two unsteady hydrodynamic phenomena suggested to contribute to the increased propulsive forces are the added mass effect and the bound vortex accompanying a shedded vortex (Samson et al. [2017]). Rouboa et al. [2006] performed simulations under steady and unsteady conditions with a hand perpendicular to the flow and found a 22.5 % increase in propulsion under unsteady conditions.

1.3.2 Stroke pattern and full stroke analysis

The arm stroke in front crawl swimming can be divided into two main patterns: the S-shaped pattern, also known as the curved pull, and the I-shaped pattern, also known as a

straight pull. The S-shaped pattern involves a stroke where drag and lift play a significant role; Counsilman [1968] first introduced the stroke. In contrast, the I-shaped pattern involves a straight pull, where drag acts primarily as a propulsive force.

According to the literature review by van Houwelingen et al. [2017a], an excessive sculling movement corresponding to the S-shaped pattern typically leads to less propulsion than a relatively straight underwater stroke and should therefore be avoided. According to a review by Wei et al. [2014], the S-shaped pattern has a longer stroke length, produces less propulsive drag, and the lift it generates is not enough to make up for the drag loss when compared to the I-shaped pattern. In the research of Takagi et al. [2015] and Soh and Sanders [2019], evidence indicates that energy expenditure is more efficient for an S-stroke, making it more interesting for more considerable distances. The I-shaped pattern is primarily used in modern professional swimming, although the S-shaped pattern is still commonly taught locally.

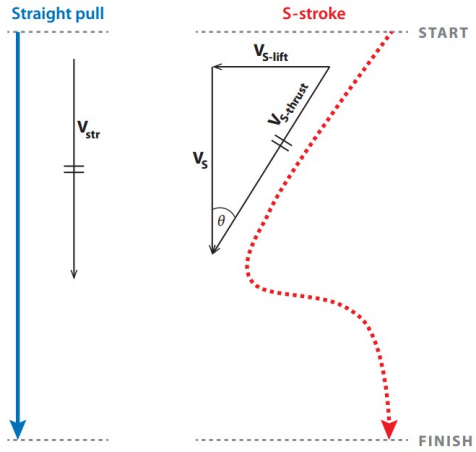

Figure 1.6.: Comparison of hand trajectories for the straight "I" and "S" stroke techniques, note that real swimming strokes are more complex, and this is only a simplified rendition, from Wei et al. [2014].

Several studies have used particle image velocimetry (PIV) and computational fluid dynamics (CFD) to analyse the mechanisms behind the different arm stroke patterns. Matsuuchi et al. [2009] used PIV to study a real swimmer. They found that a large vortex was shed due to the directional change of the hand from the pull to the push phase, with another vortex being generated and a jet flow observed between them. Using the same experimental setup Matsuuchi and Muramatsu [2011] again used PIV to study a real swimmer's stroke. It was found that the hand's orientation changes rapidly during the stroke. This resulted in a change in circulation due to the leading edge of the "hydrofoil" changing from the thumb to the little finger. This shift results in vortex generation and shedding, which then causes momentum generation.

The study of Takagi et al. [2014b] investigated the mechanism by which unsteady forces are generated in a sculling movement. To accomplish this, a male swimmer was asked to perform sculling movements using his hand, while collecting data with PIV and pressure sensors. The study's results showed that unsteady phenomena similar to those observed in the flight of insects were present during the sculling movement. When the hand moved towards the body's centre line, a pair of vortices was already present and was shed from both ends of the hand during the out-scull, rotating in the opposite direction. During the in-scull, interference between the hand and the shed vortex occurred, a phenomenon known as "wake

capture." As opposed to a quasi-steady state, the resulting force was doubled.

A more realistic analysis of different arm-pull styles was conducted in the paper of Takagi et al. [2014a], using particle image velocimetry (PIV) and force measurements with a five-degrees-of-freedom robot arm. They discovered two distinct mechanisms for drag generation. For the S-shaped stroke, an unsteady lift force was observed due to the change in movement direction during the stroke (from the insweep to the upsweep), resulting in vortex shedding and the creation of a bound vortex. A jet flow between the shed and bound vortex could be observed, contributing to the thrust. In contrast, the straight pull generated a Kármán vortex street, which shed alternately from the thumb and little finger with a jet flow in between, resulting in a quasi-steady state drag force contribution.

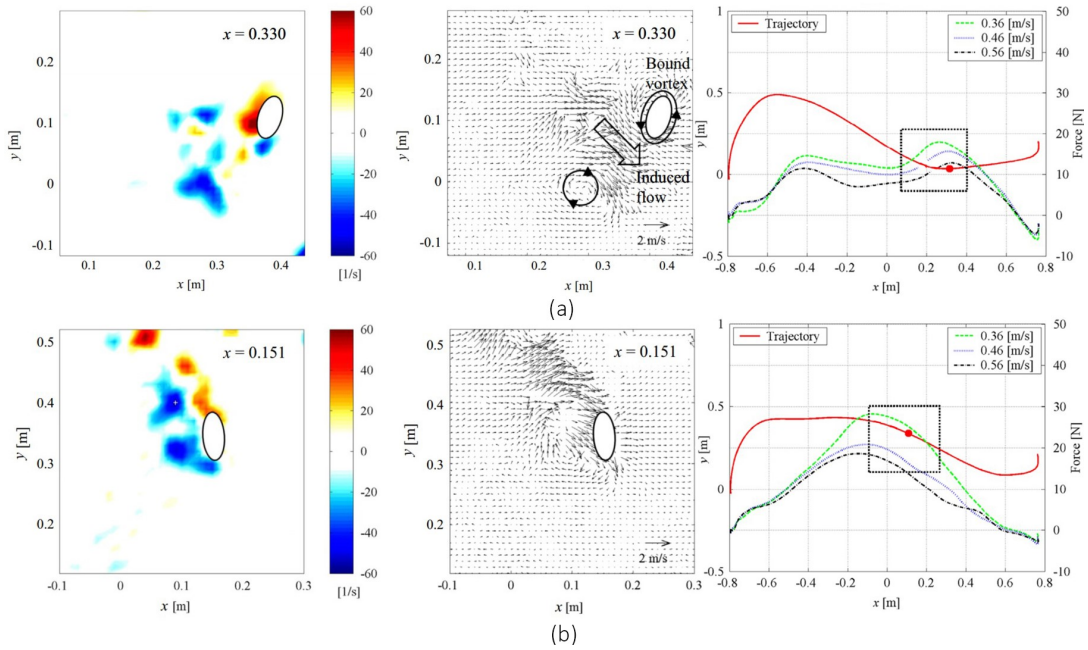

Figure 1.7.: Different fluid mechanics for the S-stroke (a) and I-stroke (b), visualised with PIV, by Takagi et al. [2014a]. Left: vorticity [1/s], middle: flow field [m/s] and right: the stroke pattern [m]

Sato and Hino [2013], tracked the middle finger of two Olympic swimmers competing in the 200 m freestyle using video footage. They found two sets of stroke paths, seen in Figure 1.8. It is remarkable how much the stroke paths differ, where the stroke path of the red swimmer resembles the straight pull, and the stroke path of the blue swimmer shows a stroke with more apparent sculling.

1.3.3 Typical velocities & accelerations

Next to following a complex path, the swimmer's velocity is not constant during the stroke. Large velocity variations are observed during the propulsion phase, which supposedly influences the force generation. Kudo et al. [2013] tracked three competitive swimmers' velocity, acceleration and pressure forces. They found a magnitude of the velocity of the hand of around 0.98 to 2.96 $\mathrm{m\,s^{-1}}$, and accelerations of 16.41 to 28.10 $\mathrm{m\,s^{-2}}$. Kinematic data from Sato and Hino [2013] show that the relative backward velocity of the hand is around 1 $\mathrm{m\,s^{-1}}$

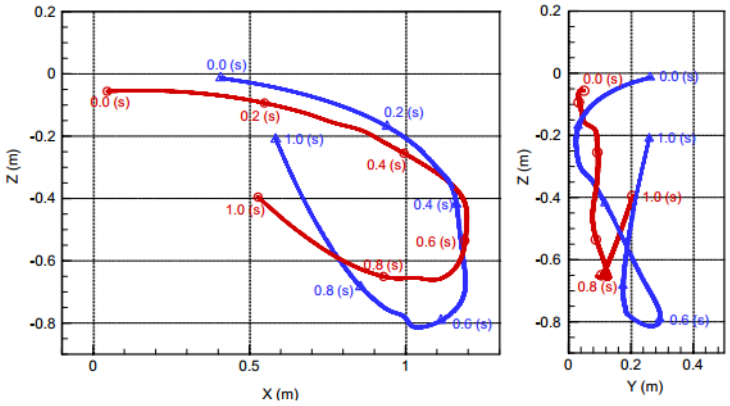

Figure 1.8.: Stroke path of two Olympic swimmers competing in the 200m freestyle, Sato and Hino [2002].

to $2\,\mathrm{m\,s^{-1}}$. Also, the absolute hand velocity lays around $3\,\mathrm{m\,s^{-1}}$ to $4\,\mathrm{m\,s^{-1}}$, with accelerations up to $18\,\mathrm{m\,s^{-2}}$. According to Sidelnik and Young [2006], the slip speed of the hand, which is the relative velocity between the hand and the water in the direction of the swimmer's forward movement, lies between 0.1 to $0.6\,\mathrm{m\,s^{-1}}$.

1.3.4 Finger spacing

The impact of finger spreading during front crawl swimming has been thoroughly examined in past research. However, most studies only looked into the generated drag force while ignoring the lift force. The difference in finger spreading is schematically shown in Figure 1.9.

The initial investigation into the influence of finger spreading in water channels was conducted by Schleihauf [1979]. The study included steady-state experiments that tested various angles of attack. It was discovered that a closed hand resulted in a higher drag coefficient C_D, regardless of the angle of attack α.

Sidelnik and Young [2006] experimented with a sculling motion performed by a two-axis robot, which performed transverse sculling. The robot was situated on a cart undergoing a longitudinal motion. While the rolling motion's dynamics were kept constant, the pitch angle, θ was varied, with pitching angles from 20° to 50°. Two hand configurations were investigated, one closed and one with a finger spread of 10°. They found that finger spacing of 10° increased propulsive forces for all pitch angles.

Minetti et al. [2009] simulated eight hands with different finger spacings at steady state velocities between $1,5$ to $3\,\mathrm{m\,s^{-1}}$. They found that a 12° finger spread resulted in an 8.8 % increase in the drag coefficient compared to a closed hand. The simulations were performed at different constant velocities, and the results were velocity independent.

Marinho et al. [2010] found a slight increase in the drag coefficient (C_D) for a small finger spread at various angles of attack. They reported an increase of 5.5 % of the drag coefficient from an initial value of 1.1 for the closed hand. A decrease in the drag force could be observed at a larger finger spread.

van Houwelingen et al. [2017b] found a positive influence of small finger spread on the drag coefficient of 2 % and 5 % in numerical simulation and experiments, respectively, compared to closed fingers. They also found a 10 % increase in the force moment at an optimal finger spread of 10°.

While performing steady-state towing tank experiments, Bazuin [2018] found a tiny improvement in the drag coefficient for a small finger spread of 5° of 1.4 %. The thesis of Bihan [2020] investigated the effect of finger spreading while performing linear acceleration, followed by a period of constant velocity. Using PIV and force measurements to analyse the results. During the initial acceleration phase, force signals were equivalent for different finger spreading. However, for the constant velocity phase, the closed hand had a significantly higher drag coefficient for different values for acceleration and velocity.

The review of van Houwelingen et al. [2017a] concludes that a small finger spread benefits a swimmer's performance. It remains unclear if this is due to vortical structures in the wake or a blockage effect between the fingers.

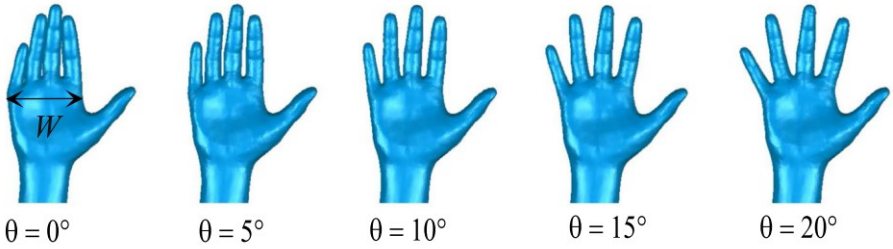

Figure 1.9.: Different hand configurations for various amounts of finger spreading, from van Houwelingen et al. [2017b].

1.3.5 Thumb position

Several studies have investigated the effect of thumb positioning on drag in front crawl swimming. Most studies want to determine if an abducted or adducted thumb generates the most propulsion.

Takagi et al. [2001] conducted a study that compared the drag coefficients of an adducted thumb to an abducted thumb. The results showed that the abducted thumb had a higher drag coefficient.

Marinho et al. [2009] used computational fluid dynamics (CFD) to simulate the effects of three different thumb arrangements (fully abducted, partially abducted, and adducted) at various angles of attack. The results showed that the adducted thumb had a 5 % higher drag coefficient than the other two thumb arrangements at all angles of attack. However, the lift coefficient was higher for the abducted thumb.

van den Berg et al. [2021] conducted wind tunnel experiments and numerical simulations to study the influence of thumb spacing on drag. They found that the abducted thumb had a higher drag coefficient, consistent with the results of Takagi et al. [2001].

1.3.6 Hand orientation

The arm and hand orientation with respect to the flow direction is important to maximise drag and lift forces. As shown in Figure 1.2b, the arm rotates in three main directions during a swimming motion, and the rotation categorised by the angle of attack (α) significantly influences the propulsion.

van Houwelingen et al. [2017a] reviewed various studies comparing the angle of attack and found that the maximum drag coefficient occurs when the hand palm is oriented perpendicular to the flow ($\alpha = 90°$), which maximises the projected area A_p. At $\alpha = 90°$, all studies' lift coefficient is close to zero. The lift coefficient becomes larger for a leading thumb

and smaller for a leading little finger. The impact of the angle of attack can be seen in Figure 1.10.

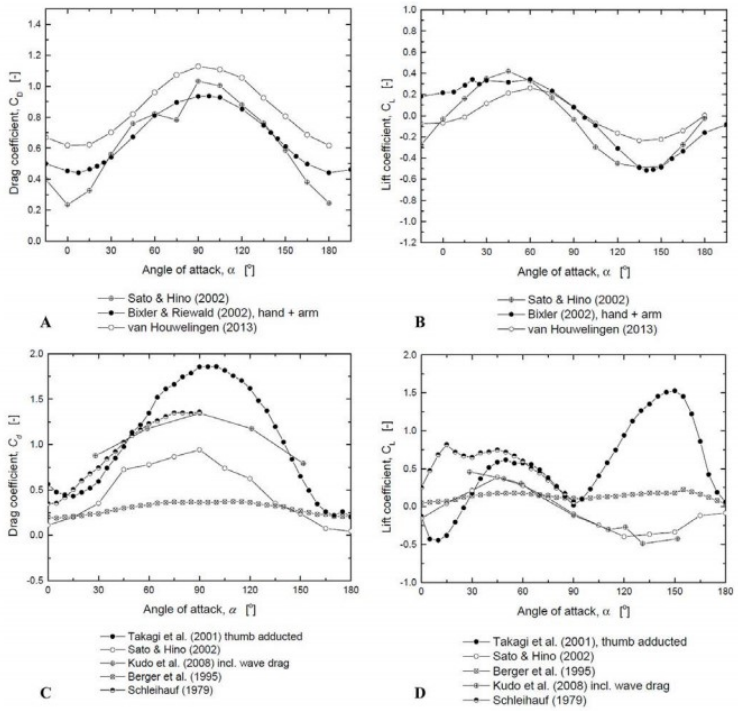

Figure 1.10.: Drag and lift coefficients as a function of the angle of attack α for numerical **A**, **B**, and experimental **C**, **D**, studies. For all studies, the sweepback angle, γ, which is the angle between the flow direction and the arm, perpendicular to the hand plane is set to 0. van Houwelingen et al. [2017a].

1.4 Scaling

Scaling is a technique used in fluid mechanics to accurately mimic real-life situations when there are limitations to the experimental setup. All relevant parameters are scaled equally to achieve similarity, ensuring that dimensionless numbers in both the original and scaled versions are equal. As the robot cannot fully replicate the high acceleration and deceleration involved in swimming and due to the geometric constraints of the tank, some scaling must be applied.

1.4.1 Reynolds independent scaling

The investigation of Grift et al. [2021] shows that for a turbulent flow around a flat plate, the force behaviour is independent of the Reynolds number. This is known as Reynolds independent scaling and is practical if constraints to the experimental setup prevent the replication of a real-sized case. In their review, van Houwelingen et al. [2017a] analysed several studies investigating the relationship between the drag and lift coefficients and the Reynolds number. Results showed that there was no dependence on the Reynolds number, which is consistent with the findings of Grift et al. [2021]. This generally means that the force can be

scaled with U^2. However, due to the forearm's cylindrical shape, it cannot be assumed that the drag and lift coefficients will remain constant at higher Reynolds numbers; at Reynolds numbers around $3 \cdot 10^5$, the boundary layer separates and becomes turbulent, resulting in a sudden decrease in the drag coefficient known as a drag crisis, see paragraph 1.2.2 (Kundu et al. [2016]).

1.4.2 Blockage effects

If a fluid comes near an object and there isn't enough room for it to move away because of nearby walls, the fluid speeds up. This causes more drag to be generated. According to a study by West and Apelt [1982], the blockage ratio ϕ (defined as the ratio of the object's area to the cross-sectional area perpendicular to the object's motion) can be up to 6 % without significantly affecting the drag during the motion of an object through a fluid. Many wind tunnels have size restrictions, so correcting for blockage effects is a commonly used technique. Extensive literature on these correction methods is available, and the thesis research of Bin-Khalid and Suda [2020] explored various approaches on a hand suspended in a wind tunnel.

Maskell [1963] developed a correction model for bluff bodies and flat plates. The model is based on the conservation of momentum between an unperturbed upstream section and a section downstream in the wake,

$$\frac{C_D}{C_{D,c}} = \frac{q_c}{q} = 1 + \epsilon * C_D * \phi \tag{1.10}$$

with $C_{D,c}$ the corrected drag coefficient, q_c/q the ratio between the uncorrected and corrected dynamic pressures and ϵ an empirical blockage factor; in the case of non-lifting bluff bodies ϵ is estimated to equal 2.5.

The model developed by Maskell [1963] fails to consider the effect of wake distortion. The extended Maskell method developed by Hackett and Cooper [2001] introduced said effect.
Thom and Herriot developed a correction model for the aeronautical industry based on potential flow theory. This model represents the wake as a source and a sink downstream. The derivation of both models can be found in Appendix A.
All models are initially intended for a wind tunnel; scaling to a water tank is possible, but the models might underestimate the result due to a free surface present.

1.5 Research objective

When it comes to front crawl swimming, there are two main patterns: the S and I-shaped strokes. The curved pull is believed to use lift and drag to move through the water; calculations by Wei et al. [2014] show that the lift cannot compensate for the lost drag with the curved pull. Despite this, the curved stroke is said to increase energy efficiency. Furthermore, analysis performed by Sato and Hino [2013] shows huge variation in stroke patterns, even at the Olympic level.

The current study aims to examine how lift affects a swimming stroke. To accomplish this, we will utilise a new robot arm with six degrees of freedom. This robot arm has to be tested, and one of the main inquiries is whether it is well-suited for this task.

As part of the first phase of this thesis research, we will gather qualitative lift coefficients for an abstract hand and arm model using both analytical and numerical methods.

We will conduct experiments on 3D-printed hands submerged in a water tank to further investigate. A force sensor will be used to measure drag and lift forces while varying the angle of attack to analyse the steady-state and transient behaviour of a swimming stroke.

Additionally, hands with different finger spreading will be compared. No prior research has been performed on these particular cases.

PIV measurements are conducted on cases where lift has the strongest impact. These measurements explore the hydrodynamic phenomena of finger spreading and acceleration during a stroke. Additionally, the aim is to establish a relationship between the lift forces determined by circulation in the two-dimensional plane and those observed in the three-dimensional experimental and numerical results.

The final chapter aims to compare simplified versions of the two-stroke styles and determine if the conclusions from earlier chapters remain valid in a more dynamic scenario.

2. Analytical model of a swimming arm

Due to the complicated nature of fluid mechanics, it is often necessary to make simplifications; this chapter introduces a simplified model of a forearm and hand, which might say something about the angle-dependent lift coefficient $C_L(\alpha)$. The simplification is achieved by slicing a three-dimensional hand and forearm model into ten equally spaced sections along its length and approximating each cross-section with an ellipse. Each ellipse is characterised by its semi-major axis (a_1), semi-minor axis (a_2), and angle (η), which is defined as the angle between the semi-major axis and stream direction perpendicular to the palm of the hand.

This chapter starts with an analytical method in the form of potential flow theory. Next, the more advanced panel method with boundary layer analysis is introduced. Expressions for the lift of simple 2D forms can be obtained using either method. Finally, numerical investigations are conducted on the simplified model.

Figure 2.1 illustrates the slicing process, while table 2.1 presents the resulting parameters, including the eccentricity ($\beta = (a_1 - a_2)/(a_1 + a_2)$).

Table 2.1.: Semi-major (a_1), semi-minor (a_2) axes, the angle between the semi-major axis and stream-direction perpendicular to hand palm (η) and eccentricity (e) of each approximated hand or arm intersection. The first six ellipses are considered to be part of the arm, while ellipses 7 to 10 are regarded as the hand.

n	a_1	a_2	η_i	β
1	50.46	40.46	47.3	0.110
2	42.64	36.32	47.0	0.080
3	38.30	31.07	56.0	0.104
4	32.26	27.28	70.5	0.084
5	31.42	24.23	89.0	0.129
6	33.88	22.50	89.8	0.202
7	58.75	21.55	89.5	0.463
8	48.71	15.74	82.3	0.512
9	47.45	13.36	84.1	0.561
10	35.59	9.32	89.0	0.585

Figure 2.1.: The hand and arm sliced into equivalent parts of 40 mm along the total length.

Parameterising the cross-section of the arm can lead to an attractive way to understand the angle-dependent lift force along the arm. Although potential flow doesn't account for drag forces as per d'Alembert's principle, an approximation can be achieved with the panel method, which approximates the boundary layer using a computed pressure distribution. Finally, numerical simulations can solve the boundary layer and wake and can therefore predict the model's drag coefficient.

2.1 Potential flow around an ellipse

Potential flow theory is used to simplify a flow where the flow is inviscid, irrotational and incompressible. Since there is no boundary layer due to the inviscid nature of the flow, there is no drag and no separation of the boundary layer, which would typically create a low-pressure wake. When calculating lift, the circulation within the flow is crucial. This is done using the Kutta-Joukowski formula, which considers the Kutta condition: a principle in fluid dynamics that requires the top and bottom flow around a hydrofoil to leave at the trailing edge.

Potential flow is based on the velocity potential ϕ and the stream function ψ; Both ϕ and ψ satisfy Laplace's equation, $\bigtriangledown^2\psi = \bigtriangledown^2\phi = 0$ and are the real and imaginary part of an analytical function. The two dimensional velocities in the x- and y-direction are described by u and v and can be related to ϕ and ψ via,

$$\begin{aligned} u &= \frac{\partial\phi}{\partial x} = \frac{\partial\psi}{\partial y}, \\ v &= \frac{\partial\phi}{\partial y} = -\frac{\partial\psi}{\partial x}. \end{aligned} \tag{2.1}$$

Because of the linearity of Laplace's equation, the superposition principle is valid, which enables us to describe complex flows with relatively simple elementary flows.
A circle with radius a in the complex plane, $z = ae^{i\theta}$, is mapped onto an ellipse using the conformal map ζ,

$$\zeta(z) = z + \frac{\xi^2}{z}, \tag{2.2}$$

where ξ is related to the eccentricity β, semi-major and minor axes, $a_1 = a + \xi^2/a$, $a_2 = a - \xi^2/a$. The conformal map is applied to a flow around a rotating cylinder, with circulation Γ imposed in a way that the flow leaves the geometry at the trailing edge; a specification known as the Kutta condition.

The complex potential $F(z)$ is an analytical function combining the velocity potential (real part) and stream function (imaginary part). The complex velocity, $W(z)$, is the derivative of the complex potential. Points at which the complex velocity equals zero are called stagnation points and are of special interest in calculating the resulting lift. The complex potential is given so that the cylinder is a streamline and far away from the incoming flow with velocity U and an angle α. In appendix B, a derivation of the complex potential is provided, and the result equals,

$$F(z) = U(ze^{-i\alpha} + \frac{a^2}{z}e^{i\alpha}) + \frac{i\Gamma}{2\pi}\ln z. \tag{2.3}$$

The derivation of the complex potential to the complex velocity and subsequent transformation to an ellipse gives the velocity over the ellipse,

$$U(\zeta) = \frac{dF}{dz}\frac{1}{\frac{d\zeta}{dz}}. \tag{2.4}$$

By applying the Kutta condition, Γ is determined, and by applying the Kutta-Joukowski equation, the following relation for the lift coefficient is found.

$$C_L = \frac{F_L}{0.5\rho U^2 2a_1} = 4\pi \frac{a}{a_1} \sin\alpha. \tag{2.5}$$

A special form of the eccentricity (β) is defined and related to the semi-major (a_1) and semi-minor (a_2) axes it is then inserted in equation 2.5,

$$\beta = \frac{a_1 - a_2}{a_1 + a_2} = \frac{\xi^2}{a^2}, \tag{2.6}$$

$$C_L = 4\pi \frac{1}{1+\beta} \sin\alpha. \tag{2.7}$$

The pressure coefficient over the two-dimensional shape can be analytically calculated by applying Bernoulli,

$$C_p(x) = U^2 - |U(\zeta)|^2, \tag{2.8}$$

with x the real part of ζ, U the free stream velocity and $U(\zeta)$ the velocity over the ellipse. These steps provide us with an analytical solution to the flow over an ellipse, and for each relevant ellipse, an analytical result can be retrieved by prescribing the right angle of attack and semi-minor and major axes.

2.2 Panel method

The panel method is a numerical method that discretises the surface of a two or three-dimensional object into straight panels; an example of an ellipse is presented in Figure 2.2. At each element, singularities (sources, vortices, and doublets) are introduced while adhering the flow to certain boundary conditions, like no flow crossing the object's surface. Each panel induces a velocity on itself and the other panels, which can be expressed through simple equations. These velocities are collected in a matrix, and a flow condition is defined on the surface so the flow moves tangentially along it. Combining the onset flow direction and boundary condition solves a system of linear equations for the unknown panel velocities.

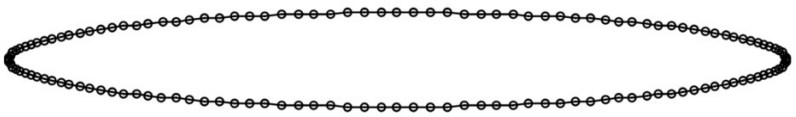

Figure 2.2.: Example of an ellipse, with an aspect ratio of eight, discretized in 140 panels.

The program *xFoil* utilises said panel method, and by setting the program to inviscid, a comparison can be made with the analytical result. Figure 2.3 displays the resulting pressure coefficient distribution, $C_p(x)$, for an ellipse with an aspect ratio a_1/a_2 of eight and an inflow angle of 20°. As the two plots match, we can conclude that the panel method is valid for this inviscid case.

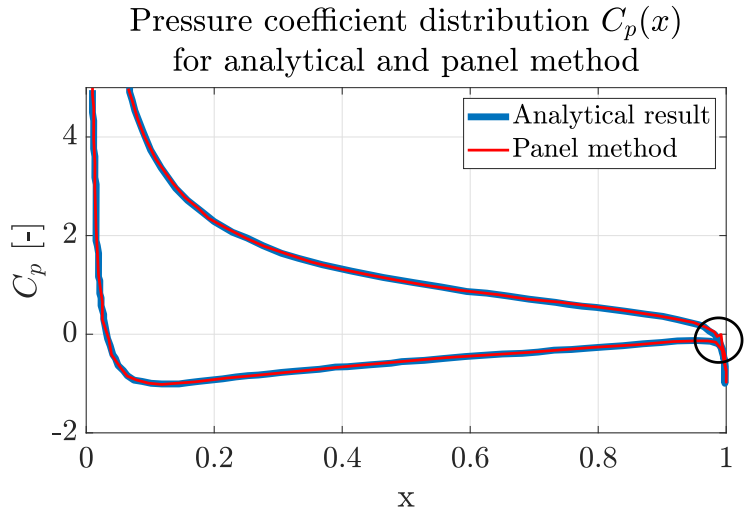

Figure 2.3.: Pressure coefficient distribution along an ellipse with aspect ratio eight and angle of attack of 20°, the methods agree for the same input case, validating both. Only at the indicated black circle, the methods don't agree.

2.2.1 Javafoil

The program *JavaFoil* uses a higher-order panel method, in combination with a boundary layer analysis, to estimate drag and lift forces along two-dimensional models. To ensure *JavaFoil's* validity, the viscosity is set to zero, and the resulting pressure coefficient distribution is compared to the previously introduced reference case. The results match and are presented in appendix B.

Higher order panel method

A higher-order panel method is a refinement of the basic panel method; the singularities are not located at discrete points on the body surface but are continuously distributed over the surface. This allows for a more accurate flow representation, leading to improved results.

Boundary layer analysis

JavaFoil calculates friction drag on geometries by analysing the viscous boundary layer; it begins at the stagnation point and solves empirical boundary layer equations along each surface. The equations are able to incorporate the effect of separation and stall up to a certain extent.

2.3 Numerical investigations

Numerical simulations are performed on a subset of the previously introduced elliptical cross-sections to gain insight into the arm and hand's lift and drag forces. The simulation will provide a global picture of the expected force distribution along the arm and hand.

The CFD program Fluent is used in the simulations, where the elliptical cross-sections are scaled 1:1 to their real-life counterpart. Temperature, water density and viscosity are taken at standard room temperature.

2.3.1 Simulation setup

In Ansys meshing, a triangular unstructured mesh is created and placed in a uniform flow, as shown in Figure 2.4. The distance labelled as D equals twice the ellipse's semi-major axis (a_1). The inlet, top, and bottom walls are situated at a distance of $8D$ from the centre of the ellipse, while the outlet is located downstream at a distance of $20D$. These distances are considered far enough to assume insignificant far-field effects.

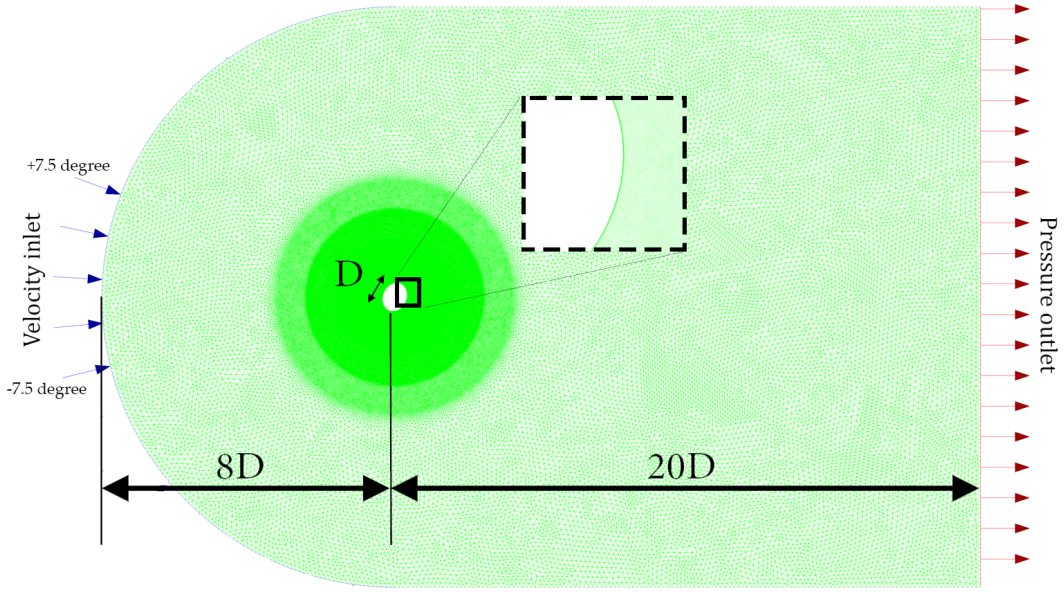

Figure 2.4.: Mesh for ellipse one

The Reynolds Averaged Navier-Stokes (RANS) equations are used as the turbulence model. Specifically, the SST $k-\omega$ turbulence model is used because it is generally superior to other RANS models. Spatial and temporal domains have a discretization set at second order upwind. The flow field is solved in steady-state using a coupled pressure-velocity solver.

A constant pressure condition is imposed at the outlet. A no-slip boundary condition is imposed on the surfaces of the elliptic shapes and on the top and bottom walls.

The force coefficients are based on two variants of the projected area A_p, either $A_{p,1}$, two times the length of the semi-major axis, $2 \cdot a_1$, equalling the used value for the two analytical methods or a variant which takes a weighted average of the semi-minor and semi-major axis, depending on the relevant angle of attack. In literature, the value $A_{p,1}$ is commonly used, but in experiments from chapter 3, the value $A_{p,2}$ is more representative of how the projected area is portrayed. Specific simulation settings can be seen in appendix C.

In order to enhance precision, certain unsteady simulations are conducted. These simulations are then utilised to compare forces to their (pseudo)-steady-state counterparts and to collect data on the shedding frequency. The transient simulations follow the same setup, with the transient formulation set at second-order implicit.

2.3.2 Simulation methods

Only a select few representative ellipses are used to reduce the number of simulations required. These ellipses, numbered one, four, seven, and nine, are chosen from table 2.1 and then scaled accordingly for the remaining ellipses. The velocity magnitude at the inlet is maintained at $0.6\,\mathrm{m\,s^{-1}}$, which corresponds to a Reynolds number of $\mathrm{Re} = 0.6 \cdot 10^5$. In order to obtain accurate data, five individual meshes are created for each ellipse to analyse the forces at different angles of attack. This results in a total of 20 meshes. The angle of the semi-major axis in relation to the flow direction is altered in increments of 22.5°, ranging from 0° to 90°. This range of angles yields sufficient data to generate a profile spanning from an angle of attack of 0° to 180°, accounting for the ellipses' symmetry. To gather additional data points, the starting angle of the incoming fluid is adjusted between −7.5° and 7.5°, following Figure 2.4.

Two different ellipses, one and nine, will be studied to observe the unsteady behaviour. Ellipse nine has a high aspect ratio, while ellipse one resembles a bluff body. Both shapes will be analysed at two angles, $\alpha = 30°$ and $\alpha = 60°$. The time step is set at $\Delta t = 0.05\,\mathrm{s}$, which is well below the expected shedding frequency. The unsteady simulations are considered while using the same incoming flow with a velocity of $0.6\,\mathrm{m\,s^{-1}}$ and a constant angle of attack. To ensure enough oscillations are present to determine the shedding frequency, at least 100 timesteps will be taken for each geometry.

2.4 Results and discussion

The analytic lift coefficient for each elliptical cross-section of the hand and forearm is determined and compared to the panel method. Following this, the results of the numerical simulations are compared to both methods. Finally, the results of the numerical simulations are extended to encompass the shedding frequencies and drag forces. In all relevant figures, an angle of attack of zero corresponds to the thumb as the leading edge, i.e. the angle η_9 equals 180°.

2.4.1 Comparison analytical methods

A comparison is made between both the analytical (PF) and JavaFoil (JF) methods. Figure 2.5a illustrates the resulting polar profile of two elliptical cross-sections, five and nine, without considering the ellipses' rotation η_i. The figure shows a matching lift coefficient C_L of up to 10° between both methods. It appears that the potential flow method overestimates the lift coefficient after this region, whereas the Panel method utilizing JavaFoil exhibits a more desirable trend, particularly for the more streamlined ellipse nine. Nevertheless, as the stall becomes more pronounced, the program finds it challenging to resolve the flow analytically.

Additionally, Figure 2.5b displays the comparison of the resulting hand and arm. The ellipses' rotation, η_i, is considered in this comparison. The provided subfigure shows how the arm's starting angle differs from the starting angle of the hand. The figure reveals that due to the more streamlined shape, the hand's lift coefficient matches well up to 7.5°; this is not the case for the arm, which due to its starting angle eta_i, already starts at a different value at $\alpha = 0°$.

The shapes are not aerodynamically streamlined enough to apply inviscid flow principles; as a result, the lift coefficient is greatly overestimated. Thus, the potential flow theory alone cannot provide a complete solution for the parameterised model. Moreover, the panel method generates a shape that has a maximum lift coefficient at low for a streamlined shape at low angles of attack. However, the result flattens at higher angles of attack and does not go to

zero. This deviates from reality. A lift coefficient of zero is anticipated at the symmetry point at 90 degrees.

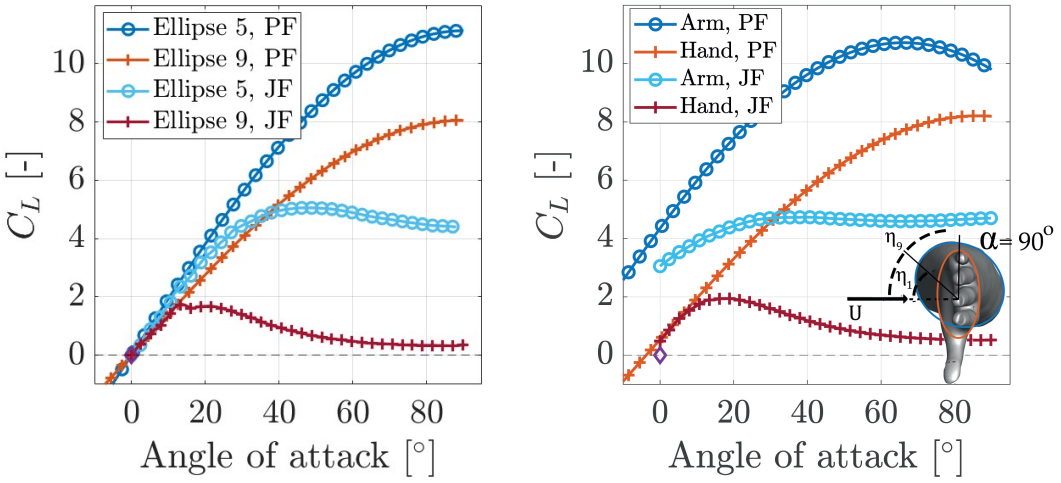

(a) (b)

Figure 2.5.: Lift coefficient against angle of attack, for a). A comparison of ellipses five and nine, shown are the potential flow (PF) and the *JavaFoil* (JF) methods. b) The same comparison for the complete hand or forearm, while taking into account the starting angle η_i of each ellipse.

2.4.2 Comparison with numerical simulations

The comparison between the numerical simulations and the advanced panel method (*JavaFoil*) is shown in Figure 2.6. A noticeable discrepancy can be observed between the two methods, particularly in the lift coefficient for the arm geometry. To enhance clarity, Figure 2.7 presents a separate graph of the numerical investigation. For the numerical simulations on the hand, the maximum lift coefficient equals 0.56, while the value retrieved from the panel method equals 1.94. For the arm, the maximum values are 0.18 and 4.72, for the numerical investigation and the panel method, respectively. The results from the literature as presented in Figure 1.10 show a comparable order of magnitude with the numerical simulations, while both analytical methods are way off. This again indicates that the analytical methods are not suited to predict the angle dependent lift coefficient $C_L(\alpha)$

Next to the lift coefficient, the numerical simulations are also able to gather insights into the angle-dependent drag coefficient $C_D(\alpha)$. The cumulative drag and lift coefficients are plotted in Figure 2.8; two different cases are presented based on the previously introduced projected areas $A_{p,1}$ and $A_{p,2}$. Results show that the maximum lift coefficients equal 0.58 or 0.31 and are found at $\alpha = 15°$, the minimum lift coefficient is found at $\alpha = 165°$ and equals either -0.52 or -0.28. The maximum drag coefficient C_D equals 1.05 or 0.96 for an angle of 15° or 0°, respectively. The simulations do not consider the potential impact of the thumb or the spreading of the fingers. The intricate variations around the hand or other three-dimensional effects are also not accounted for. Nevertheless, it is feasible to compare the outcome with experiments, which will be carried out in the following chapter.

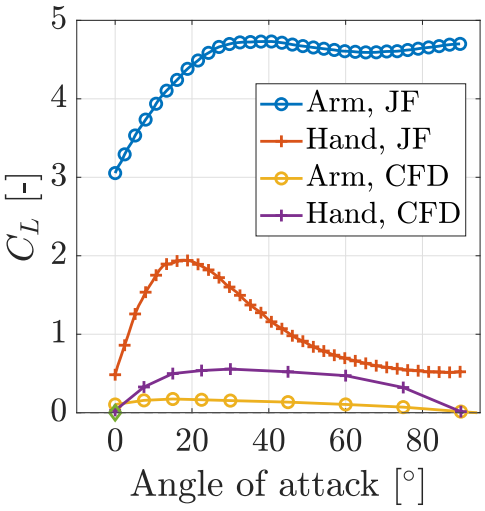

Figure 2.6.: Comparison of the lift coefficient C_L versus the angle of attack, between the *JavaFoil* method and numerical investigations. Plotted are the results for the set representing the arms and the set representing the hand.

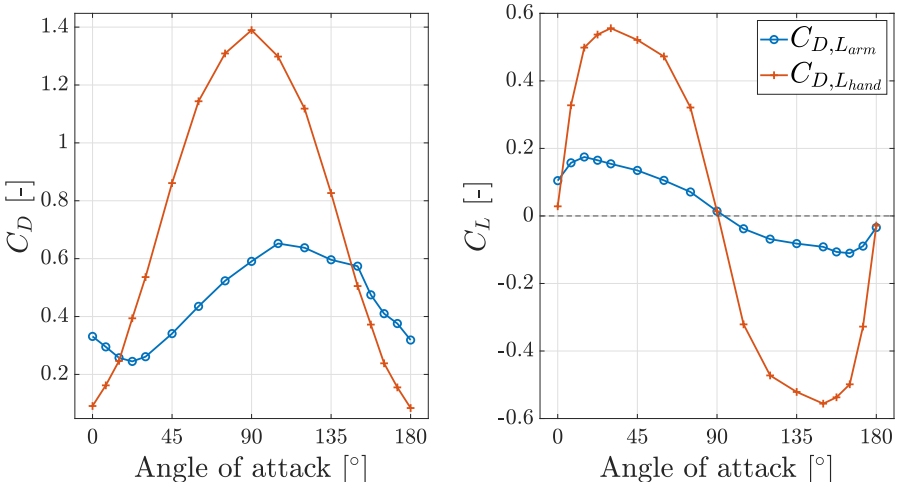

Figure 2.7.: The lift and drag coefficient, referred to as $C_{D,L_{arm}}$, includes ellipses one through six. On the other hand, ellipses seven to ten are covered by $C_{D,L_{hand}}$. This graph uses $A_{p,1} = 2 \cdot a_1$ as the projected area.

2.4.3 Unsteady simulations

Various transient simulations are performed, and the lift forces for ellipses one and nine at an angle of attack, α, of 150° are displayed in figure 2.9b. Table 2.2 presents each ellipse's shedding frequency and lift forces. The Strouhal number (St) for the bluff body ellipse is 0.23, which is relatively close to the expected value for a circular cylinder. The unsteady simulations for ellipse one took longer to reach a quasi-steady state, resulting in a smaller

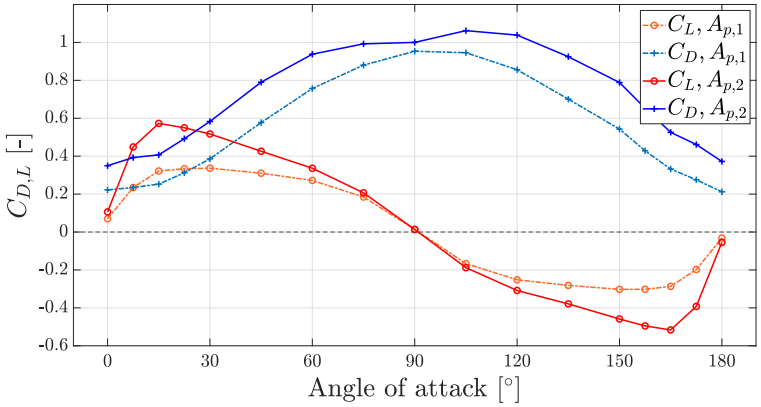

Figure 2.8.: Overall drag and lift coefficient result for all meshes while using two different methods for the projected area.

amplitude. Although the difference in lift magnitude is far smaller for the first ellipse, it is still significant. The transient lift value found for ellipse nine seems unreasonably high. More simulations should be performed to prove the validity of these results.

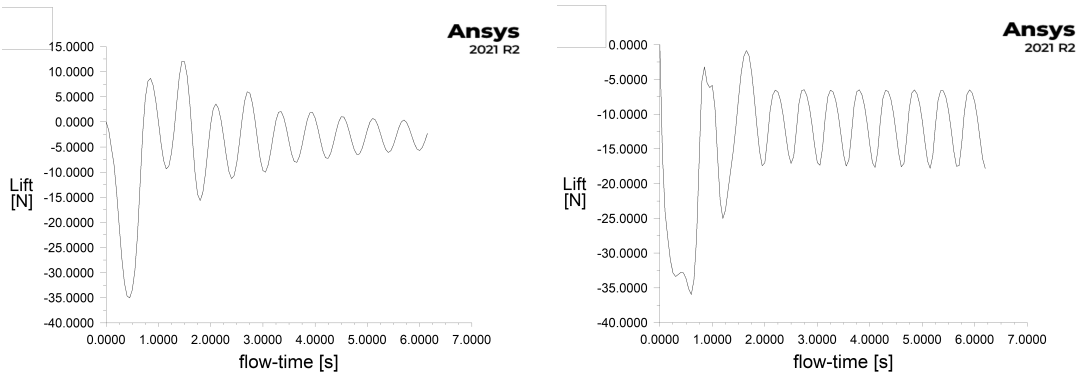

(a) (b)

Figure 2.9.: Lift force on a) ellipse one and b) ellipse nine, transient simulation to gain insight into the shedding frequency f.

Table 2.2.: Transient simulation results and comparison

	Ellipse one			Ellipse nine		
α	f [hz]	Steady-state [N]	Transient [N]	f [hz]	Steady-state [N]	Transient [N]
120°	1.76	-0.82	-2.0	1.26	-3.09	-22.5
150°	1.70	-1.83	-2.5	1.89	-3.49	-14

2.5 Conclusion

A simplification of a hand and arm model is reached by slicing the arm and approximating the resulting cross-sections with ellipses. These ellipses are then used to gather insights on the angle-dependent lift force along the forearm and hand. Two methods are used in the analysis: an analytical method based on potential flow and the panel method, which discretizes a geometry into panels, and can approximate the boundary layer using a computed pressure distribution. Additionally, numerical simulations are performed on the same abstract model.

Due to the non-streamlined shape of the arm and hand, flow separation occurs even at very small angles of attack. This flow separation is not accounted for in the inviscid analytical model, resulting in limited accuracy. Furthermore, the panel method approach forecasts stall and separation up to a certain extent. Therefore, this method can qualitatively predict the lift coefficient of a semi-streamlined shape, like the hand; however, it faces challenges in predicting the lift coefficient of bluff body shapes, like the arm. Both methods cannot quantitatively predict lift force coefficients.

Numerical simulations are performed on the simplified model, and results show a far less significant lift coefficient $C_L(\alpha)$, even at low angles of attack. Furthermore, the numerical simulations provide a clear indication that the hand's effect on the lift and drag is far greater than the forearm. Unsteady simulations are performed, and results show a significant difference with its steady-state counterpart. From these simulations, the shedding frequency is retrieved as well. In the following chapter, the resulting lift and drag coefficients will be compared to experiments with a robot arm to check the validity of the simplified model.

3. Experiments on a swimming arm

Chapter 1 demonstrates that substantial differences exist in the taken stroke path even at the Olympic level. A distinction between two strokes is made, where the curved pull uses lift and drag as forward propulsion, while the straight pull mainly relies on drag. It is generally believed that the straight pull is more favourable, this chapter will investigate whether this is true or if lift can offset the loss of drag during a curved stroke. Experiments are conducted on 3D-printed hands, with variations in the angle of attack and finger spreading. In agreement with the unstable nature of a swimming stroke, both the acceleration and steady-state phases are considered.

3.1 Experimental setup

3.1.1 Robot arm

An industrial Stäubli robot arm of the type TX2-140 with six degrees of freedom is used to conduct experiments. Figure 3.1 shows a graph of the robot arm; it processes positional and kinematic data at 250 Hz and, according to the manufacturer, has a repeatability of ± 0.05 mm. The maximum radius of the arm is 1.51 m. It is important to note that this arm is not built for research purposes and is untested. As a result, its use has certain limitations outlined in the following paragraph.

Robot limitations

Prescribing a set acceleration on the arm is impossible; instead, one specifies a percentage of the maximum allowed acceleration, which is positionally dependent. Therefore, in a stroke, acceleration is non-constant. Next, in the force signal, high-frequency noise is observed; this noise is due to interference with the lab's electrical infrastructure. In addition, a medium-frequency oscillation with a significant amplitude is observed; this noise distorts the force signal result and will be investigated in section 3.3.1.

Currently, there is a limitation in prescribing a path for the robot. It is easy to do so when moving in a straight line, but following a more complex path requires the robot to adjust the kinematics of each joint to match the prescribed velocity and acceleration profile accurately. However, initial tests have revealed that this is not always successful, resulting in unwanted accelerations during the stroke. As a result, it is challenging to interpret the force result when moving in a complex path.

3.1.2 Water tank

All experiments with the Stäubli arm take place in a rectangular tank that measures 2 meters in length (L) and 0.57 meters in both width (W) and height (H).To avoid spillage, the tank is filled to about 0.5 m. On each experimenting day, the tank's water level is checked and refilled to the appropriate depth when necessary. The room's temperature fluctuates around $21^\circ \pm 1$. This temperature variation affects the viscosity of the water, resulting in changes to its flow characteristics. The viscosity variation caused by the temperature fluctuation is roughly ± 2 %, which causes a variation in the Reynolds number of the same amount.

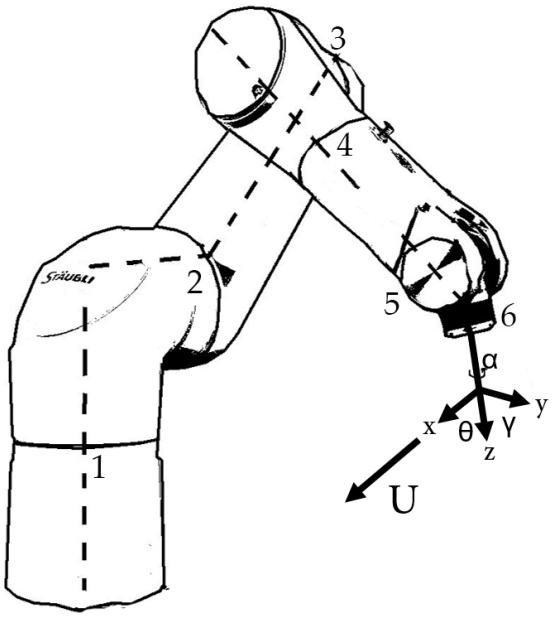

Figure 3.1.: The Stäubli robot arm with the degrees of freedom numbered one to six. Angles α, γ and θ are defined in chapter 1.

3.1.3 Hand models

Experiments are performed on full-scale hand and arm models from van Houwelingen et al. [2017b], seen in Figure 3.2b that are generated through the open source software *Make Human*. The models are 3D printed with a 2 mm wall thickness and a hollow interior. The hand palm width L_H, arm length and frontal surface area equal 0.096 m, 0.507 m and 0.042 m^2, respectively. Two hands are investigated in this research, either a hand with a 0° or 20° finger spread. Both hands have their thumb abducted as this is favourable for lift generation Marinho et al. [2009]; Vilas-Boas et al. [2015].

Initially, geometric scaling of the hands was examined, but it was determined to be impractical due to the limitations of the kinematics (the maximum robot velocity) and the length of the water tank.

3.1.4 Blockage effect

According to West and Apelt [1982], at a blockage ratio, (ϕ), above 6 %, effects of the wall are present in the force signal, and corrections should be applied. In the current experiment, the blockage ratio ranges from 9.04 to 11.3 %, which exceeds the stated limit. The experiments conducted by Bihan [2020] used a different robot arm with a blockage ratio of 3.24 %. When comparing the results to the current research, it is seen that the drag coefficient has increased by 25 % (1.05 vs. 1.32).

Several methods to correct for the blockage effect have been developed in recent years. Specifically, three methods are compared to determine which delivers the best result. These methods are Maskell's method Maskell [1963], the extended Maskell III method Hackett and Cooper [2001], and Thom and Herriot's method Bin-Khalid and Suda [2020]. In table 3.1, the outcome of the three models is presented for the reference case. The Maskell methods provided results that were reasonably close, although they underestimated the value due to

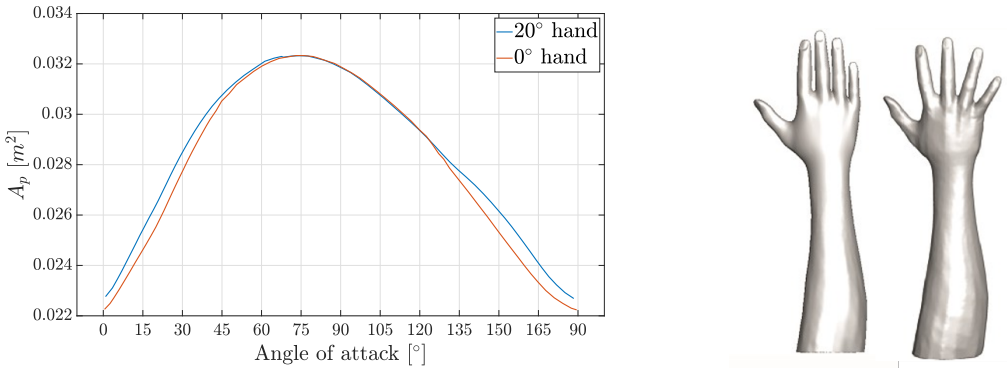

(a) (b)

Figure 3.2.: a) Projected area for the 0° and 20° hand, the hand perpendicular to the stream direction corresponds to 0°. b) model of the 0° and 20° hand

the presence of a free surface. On the other hand, Thom and Herriot's method did not seem appropriate for the current application.

Further experimentation is necessary to determine whether these correction factors are applicable for hands at all angles of attack. In the results, the extended Maskell III method is plotted along with the raw data.

Table 3.1.: Corrected drag coefficient, ($C_{D,c}$), for three different methods from an uncorrected value C_D of 1.32. The same experiment is performed with a different robot arm, which measured a drag coefficient of 1.05. Percentages indicate the difference between these two values.

Correction method	$C_{D,c}$	%
Maskell	0.963	8.28 %
Maskell III	1.016	3.24 %
Thom and Herriot's	1.207	15.0 %

3.1.5 Definition of forces

Figure 3.3 illustrates how forces are specified for all experiments. Two coordinate systems are defined: the global coordinate system $X - Y$, which runs along the length and width of the tank, and the local coordinate system $x - y$, which corresponds to the attached arm. Specifically, the palm of the hand is directed towards the positive x-axis, corresponding to a force of F_x. The force measured perpendicular to F_x is referred to as F_y.

The drag F_D and lift F_L forces are defined by the movement direction in the $x - y$ plane, the drag force F_D is defined as being opposite to the motion, and the lift force F_L is directed perpendicular to F_D in the $x - y$ plane. As the vertical lift component in the z-direction is small, it is not included in this investigation.

For the experiments in chapter 5, propulsion of different strokes are compared, and an extra propulsive force F_X is introduced along the main movement direction of the arm. F_Y is the corresponding non-propulsive component of the force.

The angle λ is the angle between the main movement direction X and the direction of

movement; it is defined as,

$$\lambda = \arctan \frac{U_Y}{U_X}. \tag{3.1}$$

The angle of attack, α, is defined as the angle between the y-axis and the velocity vector projected onto the x-y plane, i.e. the direction of the drag force. At $\alpha = 0°$, the thumb is considered the leading edge, while at $\alpha = 180^o$, the little finger takes on this role. The arm and hand are always directed straight down along the z-axis, which in turn is always at an angle of 90° with the flow direction.

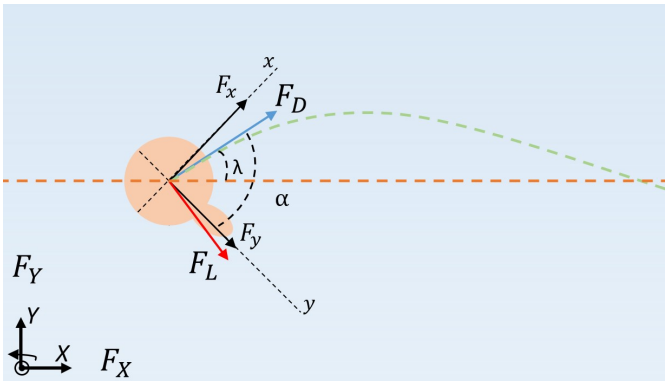

Figure 3.3.: Definition of forces, with $x - y$ the local coordinate system, and $X - Y$ the global coordinate system. The forces are decomposed in F_x, F_y, F_D and F_L, the angle of attack α signifies the rotation of the arm along the z-axis, where at $\alpha = 0$ the thumb is the leading edge. The angle λ is the angle between the main movement direction x and the velocity vector of the hand. For additional experiments involving sculling (shown in this figure), F_X is defined as the useful propulsive force and F_Y as the non-propulsive force.

3.2 Experimental methods

In the following section, the experiment is described. All investigations are repeated thrice to account for any random errors. Some experiments are repeated to see if no other errors are present.

3.2.1 Kinematics

A linear path of 1.5 m is traversed to investigate the influence of lift and drag on the models. The models are accelerated from rest up to a constant velocity of either $V_{end} = 0.45\,\mathrm{m\,s^{-1}}$ or $V_{end} = 0.6\,\mathrm{m\,s^{-1}}$, corresponding to Reynolds numbers of 0.45 and $0.6 \cdot 10^5$, which is well in the turbulent regime, but not in the region where one would expect a drag crisis ($\mathrm{Re} > 10^5$). Acceleration is kept at a constant percentage, corresponding to a varying acceleration of the robot arm between 1.5 to $1.7\,\mathrm{m\,s^{-2}}$. The velocities described resemble a hand's expected free slip velocity traversing through the water. The angle of attack is varied with increments up to 15° between 0° and 180°. For each hand and velocity, 19 angles are investigated, totalling 76 unique experiments.

To decrease the effect of the free surface on the hand, the hand models are submerged to a depth h of 0.4 m; at this depth, the distance to the tank bottom is 0.1 m from the fingertip

and the hand palms distance to the surface is about 0.2 m, the free surface effect on the hand is assumed to be negligible.

As the angle of attack varies, the projected area of the hand perpendicular to the movement direction also changes. In Figure 3.2a, the frontal surface area is presented for the 0° and 20° hand.

The forearm will be suspended through the free surface, creating additional resistance in the form of waves. The investigated velocities correspond to Froude numbers, Fr, of 0.5 and 0.7; Bazuin [2018] on a circular cylinder showed that these values correspond to a drag coefficient difference of 0.05 (from 0.62 to 0.67). Even though the arm is more elliptical, which in turn means the surface deformations would be more significant, the arm plays only a minor role due to the lower drag coefficient of the arm relative to the hand. Therefore, the C_D value of the whole arm and hand showed a relatively minor increase in the drag coefficient of 0.04 when varying the velocity. This result is deemed insignificant, given the measurement accuracy of the current setup.

3.3 Results and discussion

The experiments' results are presented in this section. Firstly, a typical force measurement is analysed and presented. Additionally, the cause of medium-frequency oscillations is described. Following this, the drag and lift forces are presented, along with the lift-to-drag ratio for both steady and transient cases.

3.3.1 Typical force measurement

In each unique experiment, the drag and lift forces on the hand are sampled at a rate of 10 kHz. In Figure 3.4, the force as a function of time is presented for a 0° hand at an angle of attack α of 30° and an end velocity $V_{end} = 0.60\,\mathrm{m\,s^{-1}}$. High-frequency fluctuations are present in the force signal. For better readability and to prevent unphysical results (e.g. dividing by zero or close to zero), the signals are filtered with a combination of a lowpass (cutt-off frequency 40 Hz, steepness, 0.99) and a moving average filter with a window size of 301 samples, corresponding to 0.03 s. The red line in Figure 3.4 represents the filtered lift signal, while the blue line represents the filtered drag force.

The drag signal shows a clear peak when the acceleration reaches its maximum at $t = 0.365$ s, Grift et al. [2019], describes this as the acceleration phase. A peak in the lift force is observed just after the acceleration phase, at $t = 0.5$ s; it is hypothesised that this peak is due to the starting vortex separating, for a velocity of $V = 0.45\,\mathrm{m\,s^{-1}}$, the same peak is observed at the same spatial position. Indicating that the peak is not velocity dependent. The lift peaks are present in most experiments, and at low and high angles of attack, they are the only region where the lift is observed to be higher than the drag. Furthermore, after 2.3 s, the observable noise seems to increase; this can be attributed to the interference of reflecting waves.

Medium-frequency oscillations

The signal displays medium-frequency fluctuations between 10 and 20 Hz. According to a study by Grift et al. [2019], these fluctuations are caused by a Kelvin-Helmholtz instability in the shear layer. This instability reveals itself as secondary vortices in the flow. Still, whether these fluctuations are due to fluid mechanics or external factors such as vibrations from the experimental apparatus is uncertain.

To differentiate between both causes, a flat plate is suspended from the robot arm, and the initial position is adjusted, ranging from −17.5 to 70 mm, Figure 3.5 displays the filtered drag force from each trial. A clear overlap is observed after two or three wavelengths, suggesting

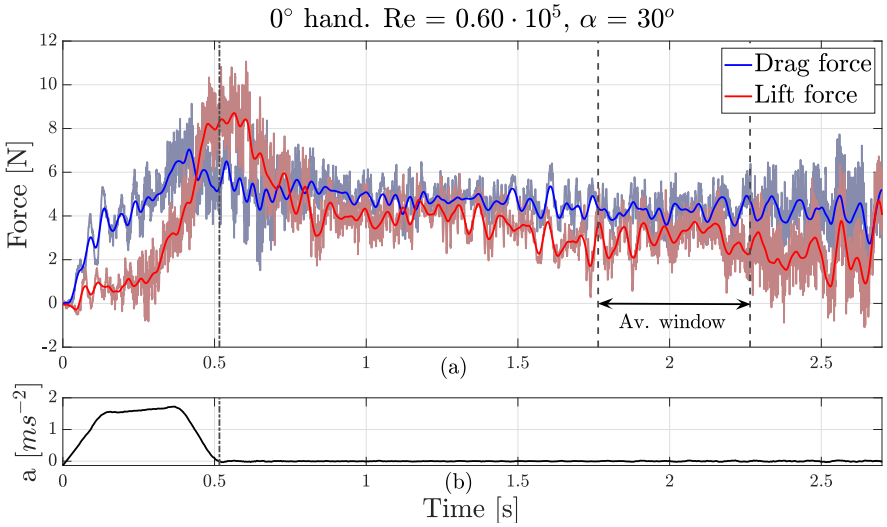

Figure 3.4.: a) A typical force signal for the drag F_D and lift F_L forces, the filtered signals are shown over the signals, and it can be observed that the filtered signal follows the raw signal well in the medium frequency area, the averaging window is where the force is deemed in steady-state. b) Acceleration profile of the hand; notice the non-constant acceleration profile.

that the medium-frequency noise is not hydrodynamic or physical but is caused by the robot's internal components or other oscillations produced by the apparatus.

To further examine the oscillations, the frequency domain is analysed. The top five highest frequency peaks that fall within the 4 to 25 Hz range are selected for each performed measurement involving the hands at varying angles of attack. In total, 54 valid measurements are performed, which in turn is the maximum value. Figure 3.6 shows the total count of each frequency within this range for both hands and a Reynolds number of $0.6 \cdot 10^5$. The blue bars represent drag, while the orange bars represent lift.

For the drag, oscillations are observed around 5 Hz, 14 Hz and 23 Hz. The 5 Hz may be due to von Kármán shedding caused by the fingers and thumb. For a circular cylinder, the Strouhal number is usually around 0.21. With the diameter of the model's fingers and thumb, this corresponds to a frequency of approximately 5 Hz.

The lift peaks are observed mainly around 13 to 14 Hz, while some peaks are present around the 20 to 25 Hz range. The figure shows more concentrated peaks for the 0° hand. The oscillations present in Figure 3.4 are 19 and 14 Hz for the drag and lift, respectively. these frequencies will be investigated further in chapter 4.

3.3.2 Repeatability

In order to ensure the accuracy of the results, the consistency of the drag and lift signals is checked. Due to the presence of high levels of noise, a comparison without filtering is not feasible. Therefore, the signals are filtered before conducting the comparison.

In Figure 3.7, an averaged drag and lift signal is presented with a solid line; the blocked lines are individual experiments' drag and lift results.

The error for the drag constituted less than 2 % for all measurements, while the value for the lift force varied along the chosen angle of attack, in general, for the experiments where lift played an important role; the error was less than 4 %.

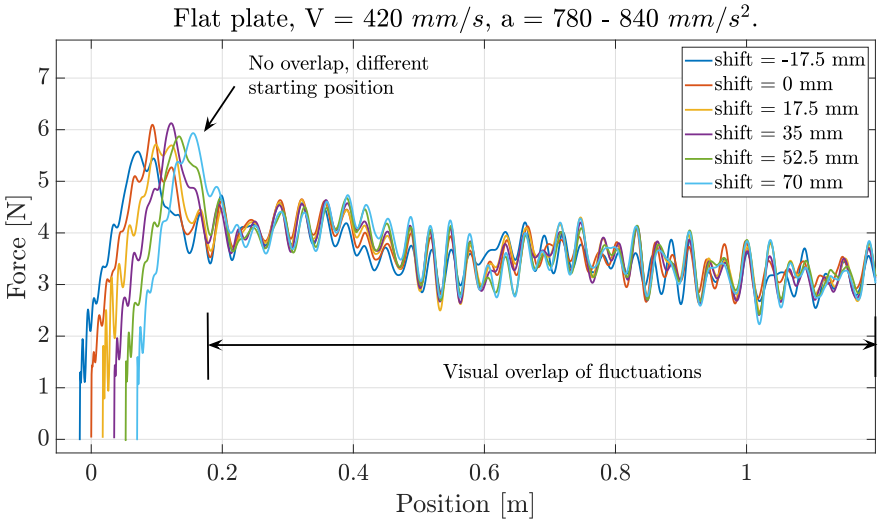

Figure 3.5.: Force against the position for a flat plate with different shifts. As can be seen, the signal overlaps after some wavelengths, indicating that the robot's internals are the cause behind the medium-frequency oscillations.

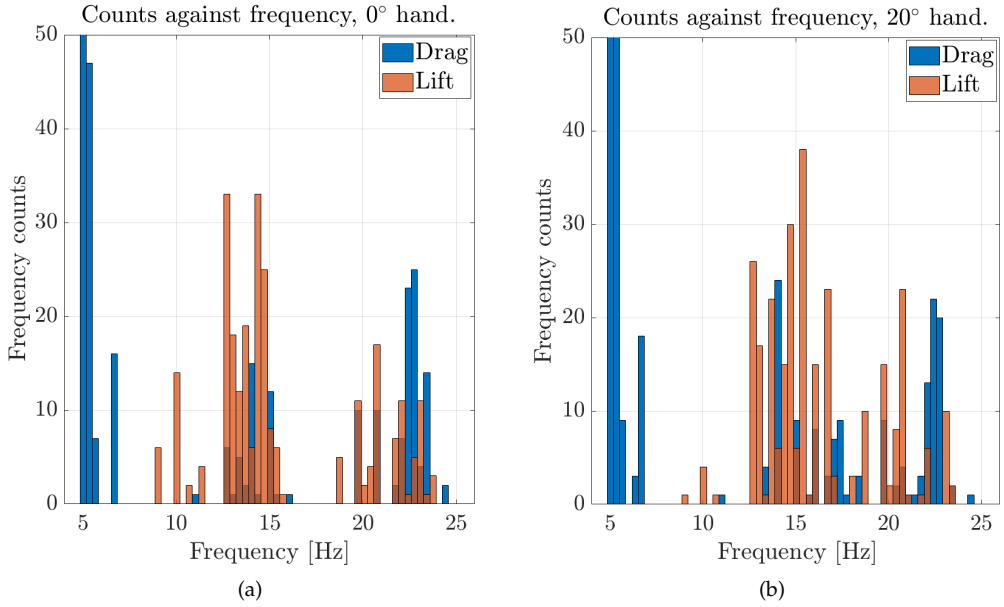

Figure 3.6.: For each valid measurement under different angles of attack, the five most significant frequencies for the lift and drag force are retrieved in the range from 4 Hz to 25 Hz. Each frequency value is counted and the total count of each unique frequency is plotted. The total amount of measurements for both hands equal 54, making that the maximum value. In blue, the drag, and in orange, the lift.

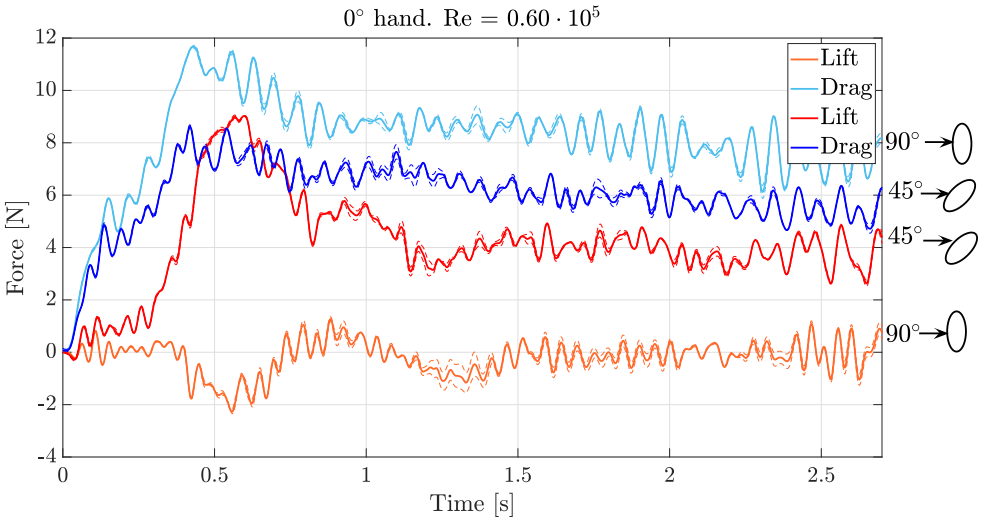

Figure 3.7.: Lift and drag forces for a 0° hand against time, for $\alpha = 45°$ and 90°. The solid line is the weighted average, while the dotted lines are individual experiments.

3.3.3 Drag and lift coefficients

From the measured drag and lift forces, the force coefficients are calculated as follows,

$$C_{L,D} = \frac{2F_{L,D}}{\rho U^2 A_p}, \tag{3.2}$$

where, the projected area is based on Figure 3.2a.

In Figure 3.8, the lift and drag coefficients of a 0° and 20° hand are plotted against the angle of attack, the end velocity V_{end} of both experiments is 0.60 m s^{-1}. The values correspond to the mean over the averaging or steady-state window, as reported in Figure 3.4. The corresponding errors are expressed as a Root Mean Square Error and are plotted alongside the mean value,

$$RMSE = \sqrt{\frac{\sum (\hat{y}_i - y_i)^2}{n}}, \tag{3.3}$$

where $\hat{y}_i$ is the mean value and n, the sample size. It is observed that the 0° hand is more favourable for the lift coefficient, while the drag coefficient depends on the angle of attack. At angles below 90°, it is clearly visible in the individual force graphs that the 20° hand has a significantly larger drag coefficient, while at angles above 90° the drag profile seems identical. According to the study conducted by van Houwelingen et al. [2017b], it is generally advantageous to have a small finger spread of around 5° at an angle of attack of 90°. This optimum lays closer to the 0° hand than that of the 20° hand. The drag coefficient is higher for the 0° hand, which supports this finding. Further experiments on different hand setups are necessary to determine the optimal amount of finger spreading for other angles of attack.

3.3.4 Comparing numerical and experimental results

Figure 3.9 shows a comparison of the corrected result with the result obtained from two-dimensional simulations. The drag coefficient exhibits small variations in the medium attack angle range, but significant variation is observed at lower and higher angles of attack. At low

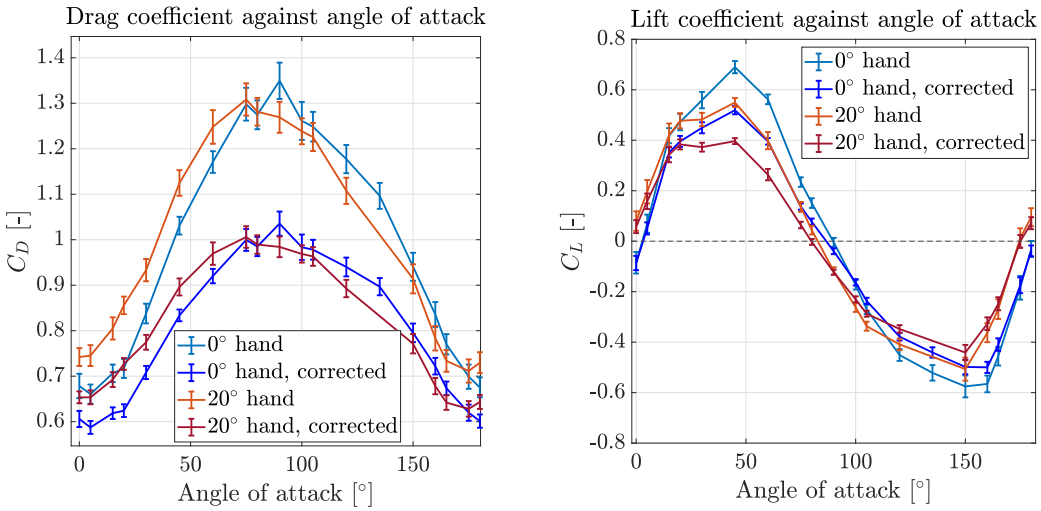

(a) (b)

Figure 3.8.: Force coefficient results for an 0° and 20° hand, with a) the drag coefficient against the angle of attack, b) the lift coefficient against the angle of attack, Re $= 0.6 \cdot 10^5$. Corrected values found via the extended Maskell III method are provided.

angles of attack, the lift peak is shifted due to the presence of the thumb as the leading edge. However, at high angles of attack, it is aligned. In a wind tunnel test conducted by Bazuin [2018], various hand cuppings were tested, and the results for a similar hand are compared with our results. The wind tunnel experiment fully immersed the arm in the flow, and no free surface was present. This may explain the observed variations between the C_D and C_L results.

3.3.5 Lift-to-drag ratio

This section presents the lift-to-drag ratios for both the steady and transient cases. These ratios provide valuable insight into the dominant force and help to quickly determine if lift can offset the drag force.

Steady-state

The graph shown in Figure 3.10 displays the lift-to-drag ratio for all investigated angles. It is important to note that the figure only shows the uncorrected result. However, the corrected result presented in appendix D, Figure D.1 shows no significant difference between the corrected and uncorrected graphs.

Figures 3.8a and 3.8b show variations in lift and drag forces between both hands, resulting in a significant difference in the ratio between angles 20° and 50°. The maximum deviation is around 0.15, resulting in a difference of 32 %. The highest ratio for the 0° hand is 0.73 or -0.7, observed at angles of 30° and 165°, respectively. For the 20° hand, the maximum ratio is observed at 15° and 150°, with values of about 0.6 and -0.6, respectively. The intersection of the x-axis is slightly different for each arm, and the force signal variations are more significant at low and high angles of attack, as indicated by the error bars.

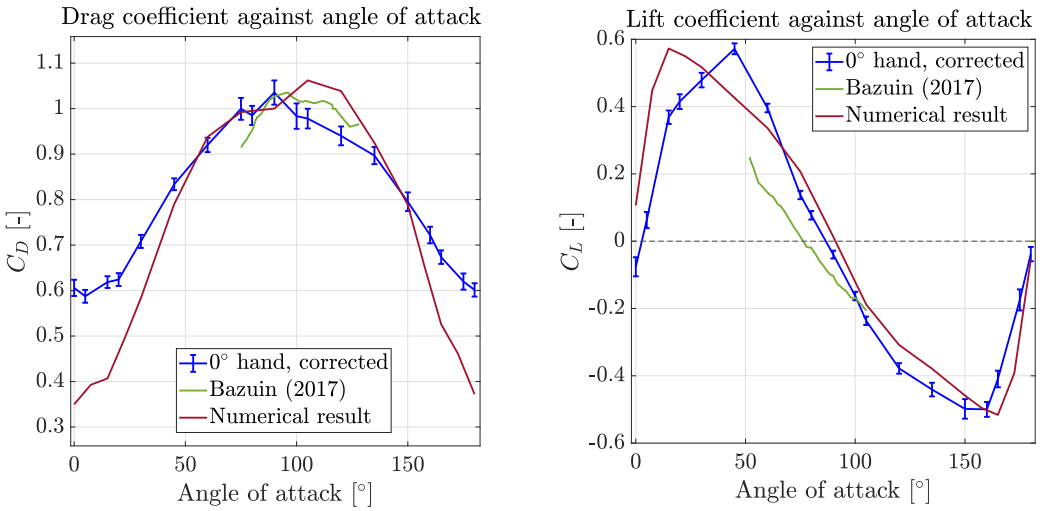

Figure 3.9.: Comparison of drag and lift forces between the experiments and the ellipse simulations. $A_{P,2}$ is used as the projected area, as this closely resembles the projected area used for the 3d geometry (figure 3.2a).

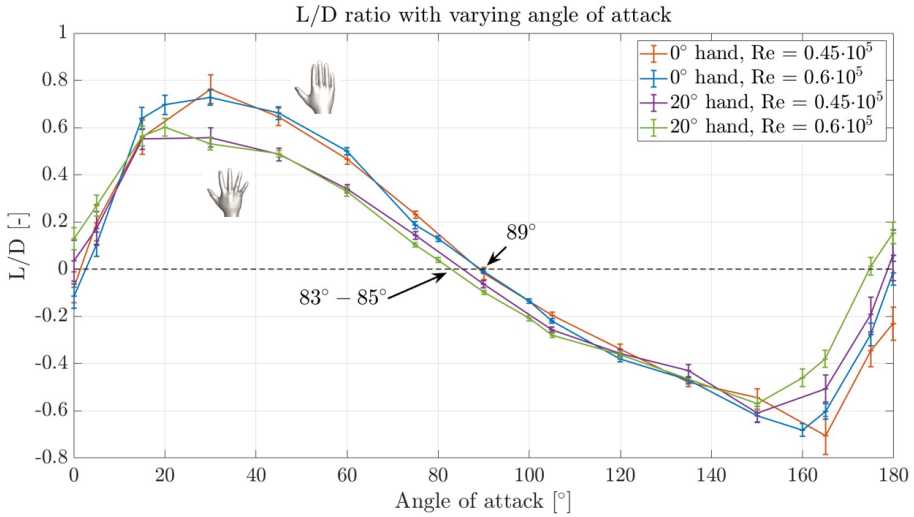

Figure 3.10.: Polar profile of steady state lift-to-drag ratio against the angle of attack for a 0° hand (red and blue) and a 20° hand (purple and green).

Transient

Following section 1.2.4, one would expect a lower lift force due to the *Wagner effect*, which states that the starting vortex negatively influences the bound circulation along a hydrofoil. However, as shown in Figure 3.4, the opposite occurred with a lift peak observed at $t = 0.5\,\text{s}$. It is possible that dynamic or delayed stall is responsible, where an attached vortex is created

and shed at the leading edge, and it reattaches, forming a leading-edge bubble. The shedded vortices are substantial, resulting in a sizeable pressure difference and a consequent lift peak. In all experiments, a peak is consistently observed. Figure 3.11 displays the Lift-to-drag ratio of these peaks against the angle of attack for both hands and a velocity of $0.6\,\mathrm{m\,s^{-1}}$. The figure includes the steady-state ratio to highlight the differences between the two regions. The graph reveals that lift exceeds drag only during the transient lift peaks. The maximum lift peaks of 1.54 and -1.68 occur at 20° and 150°, respectively.

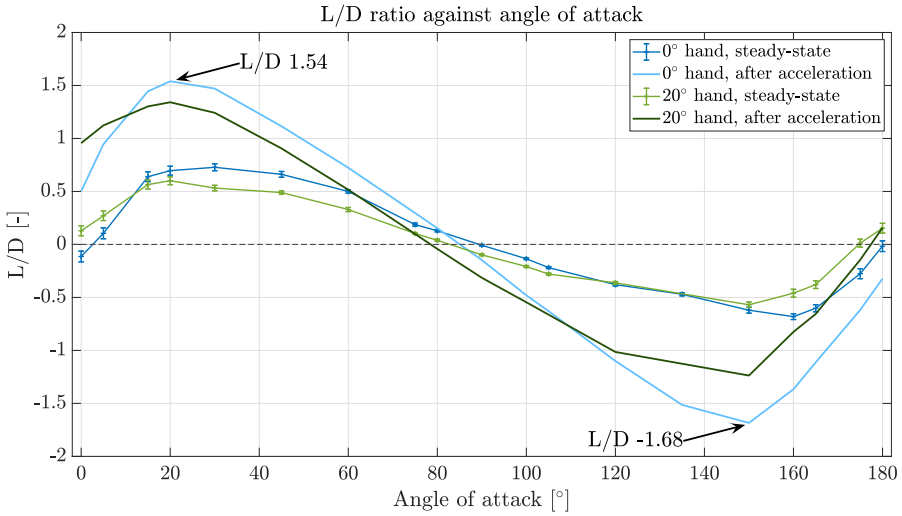

Figure 3.11.: Lift-to-drag ratio against the angle of attack, $\mathrm{Re} = 0.60 \cdot 10^5$. The graph shows both the transient and steady-state behaviour.

3.4 Conclusion

Experiments are performed with a new 6-DOF robot arm, and a medium-frequency oscillation is found to stem from the robot. Furthermore, limitations on the acceleration input and the following of complex paths currently exist. The steady-state outcomes are prone to significant errors based on the observed oscillations and the short distance covered. As a result, it is recommended that such tests be conducted in wind or water tunnels. However, the configuration is ideal for assessing more dynamic movements, provided the current challenges are addressed first.

The found blockage ratio exceeded the ratio where wall effects can be expected. This was caused by the combination of the small tank and the real-life size of the hands. Correction methods were investigated, and the Maskell III method seems the most promising. Additional experiments should be conducted, such as varying the submerged depth, scaling the arm or increasing the tank size, to determine the method's accuracy further or be able to neglect the method entirely.

While a quantitative comparison with literature may not be feasible, comparing both hands is possible. The comparison showed variations in drag and lift forces which are interesting to investigate further. Experiments are conducted on two hands with different finger spreading. The angle of attack was varied to observe the lift and drag response under a steady and transient state. Results showed that a 0° hand generally is favourable for lift, while drag

depends on the angle of attack. The resulting lift-over-drag ratio favours the 0° hand, which is more suited for a sculling stroke. After an impulsive start, there are noticeable peaks in lift, which may be caused by a delayed stall. The upcoming chapter will analyse these findings, while using PIV.

4. Flow field around a hand cross-section, using PIV

In this chapter particle image velocimetry is used to observe the flow pattern around a hand. The main focus is on lift force as a propulsive force, and thus PIV is applied to a couple of cases from chapter 3 where lift force was highly prevalent, being that at very high and very low angles of attack. Additionally, the influence of finger spreading and transient behaviour will be investigated.

When taking a broader perspective, it seems improbable that employing these extreme angles in a swimming stroke will lead to greater forward propulsion. Nonetheless, studying these extreme cases can provide valuable insights and help understand why lift and consequently sculling are not advantageous for the front crawl.

4.1 Experimental setup

Figure 4.1a shows the planar PIV setup, which is positioned around the glass tank to measure the flow field around the hand. A high-speed CMOS camera (LaVision Imager pro-HS, 1 Megapixel) is placed below the glass tank, directed upwards in the z-direction; to get a time-resolved result, the flow field is captured in single frame mode, with a frame rate of 1.28 kHz. The camera's memory capacity limited the total image time, which can hold up to 3124 frames per individual experiment. The total time of each measurement thus amounts to 2.44 s. A summary of the relevant PIV parameters is found in appendix E.

Particle seeding

To capture the flow field around the hand, neutrally buoyant fluorescent tracer particles, (*Cospheric* UVPMS-BR-0.995), with a diameter range of 53 to 63 µm are dispersed in the glass tank. The particle material is polyethylene, and the particle density is $0.985 - 1.005\,\mathrm{g\,cm^{-3}}$. The Stokes number is a dimensionless number relating the characteristic time scale of a droplet or particle suspended in a flow to the characteristic time scale of the flow; in other words, it relates the time of changes in the fluid flow to the time it takes to react to changes. It is defined by,

$$\mathrm{St}_p = \frac{\tau_p}{\tau_f}, \tag{4.1}$$

where τ_p is the characteristic time scale of the particle and τ_f is the characteristic time scale of the object; in the current study, τ_f is defined as the ratio between the characteristic length scale of the object L_h, being the width of the hand in the relevant plane divided by the steady-state velocity, U. τ_p is defined as,

$$\tau_p = \frac{\rho_p d_p^2}{18\nu\rho_f}, \tag{4.2}$$

where ρ_p is the particle density, d_p is the particle diameter and ρ_f is the density of the fluid. When the Stokes number is less than 0.1, the suspended particles are assumed to follow the flow and its characteristics sufficiently. Filling in the equation,

$$\mathrm{St}_p \cong \frac{(6.3 \cdot 10^{-5})^2}{18 \cdot 10^{-6}} \cdot \frac{0.6}{0.1} \cong 1.32 \cdot 10^{-3}, \tag{4.3}$$

meaning that the particles follow the flow. The purpose of the fluorescent particles is to convert the incoming light into light of a different colour Adrian and Westerweel [2011]. In this way, the seeded particles can be distinguished from the scattered light of the investigated solid objects (the hands). The emitted light of the fluorescent particles under a light source with wavelengths between $300 - 550\,\mathrm{nm}$ is red. In order to achieve a subsequent tracer image, a particle density of approximately eight particles per 32×32 px. interrogation window is selected. When considering a water tank with a volume of $0.57\,\mathrm{m}^3$, this equates to $2 \cdot 10^5$ particles per square meter. To avoid over-saturating the liquid, the particles are gradually dispersed in small amounts, with a final amount of approximately 8 grams dispersed, resulting in a density of about $1.6 \cdot 10^5$ particles per square meter.

Laser sheet

The fluorescent particles are illuminated by a strong homogeneous laser beam (527 nm Nd-YLF laser, *Litron* LDY300-PIV). To illuminate the particles, the laser beam is split, and a pair of overlapping opposite laser sheets are produced using a set of lenses and mirrors. The thickness of the laser sheet is set at approximately 1.5 mm because of the particles' unknown out-of-plane motion, which can significantly interfere with the observed correlation, especially with a complex shape like a hand. Splitting the laser beam results in a more thorough illumination from two opposite directions, preventing the hand's shadow from interfering with the perceived flow field. The double-pulsed laser has been set at single exposure mode, which effectively matches the frequency of the laser pulse to that of the camera's frame rate.

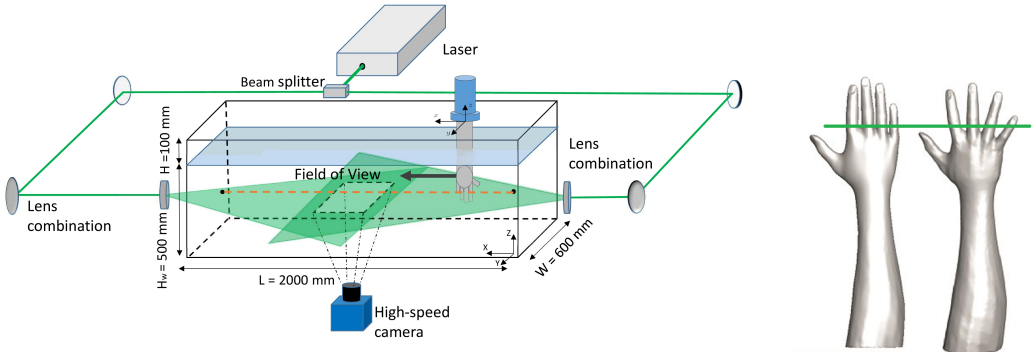

Figure 4.1.: a) PIV setup along the glass water tank. b) The investigated arm, with the green laser sheet positioned just above the hand palm.

4.1.1 Post-processing

In post-processing, a multiple-pass interrogation method is chosen; the initial and final interrogation window his set at 32×32 pixels and 16×16 pixels, respectively. The interrogation window's overlap is set at 50 %. As a guideline, the one-quarter rule states that the interrogation window should be four times larger than the particle displacement for a good

correlation, Adrian and Westerweel [2011]. This rule is slightly exceeded in the current setup, meaning correlation should be closely monitored.

4.2 Experimental methods

The camera's field of view is adjusted to obtain a xy-plane of around 335×335 mm. With a 16×16 pixels interrogation window and 50 % overlap, this corresponds to a vector spacing of 1.32 mm, which is deemed a sufficiently small scale for relevant fluid phenomena. Due to the close proximity of the camera and the hand, the hand is warped as it moves through the field of view, and precautions are taken to ensure the validity of results in post-processing. The laser plane cuts the hand through the proximal phalanx, as shown in Figure 4.1b; this height is chosen as all fingers excluding the thumb of both hands are still visible in the laser plane.

In order to analyse both the transient and steady-state responses, the initial starting position of the hand was altered. The starting positions were either just before the field of view or at a distance of 750 mm before. The angles are chosen based on the force measurements where the lift played the most significant role, namely 30° and 150°. Every experiment is performed on two different velocities, totalling sixteen unique experiments. Please refer to appendix table E.2 for a complete overview of the experiments.

4.3 Results and discussion

Experiments with the 0° and 20° hands are performed on two angles of attack; in the following section, a couple of cases are compared; these cases try to encompass the variation in finger spreading and the difference between the transient and steady-state case. Next to this, lift forces determined by circulation in the two-dimensional plane are related to those observed in the three-dimensional experimental and numerical results.

4.3.1 Difference in finger spreading

Figures 4.2a shows the vorticity result of a 0° hand, while Figure 4.2b shows the result for a 20° hand. In both experiments, the Reynolds number and angle of attack are $0.60 \cdot 10^5$ and 30°, respectively. The shown window corresponds to the steady-state forces shown in Figure 4.3. This plot shows a difference between both hands' lift and drag force. In the steady-state window, a drag difference of 15 % is observed, while the lift difference equals 10 %.

The driving force behind the lift is the pressure difference across both sides. Gaps in the hydrofoil reduce said pressure difference, decreasing the effectively generated lift. Furthermore, small jets are formed between the spread fingers, bringing higher fluid momentum and increasing local drag generation. Both phenomena are visible in the two-dimensional plane and can explain the found three-dimensional force discrepancy between both hands. Next to the small formed jets, a wider disturbance is created by the 20° hand. This broader wake is clearly visible at a chord length away from the hand, suggesting greater turbulence.

4.3.2 Explaining the lift peak

Figure 4.4 displays the vorticity fields of a 0° hand with a 30° angle of attack. The figure depicts two cases: one where the hand is accelerating and one where it reached a steady state, both at a consistent velocity of $600\,\mathrm{mm\,s^{-1}}$. A comparison of the two cases reveals differences in the wake created by the hand. The transient case has a narrower and more concentrated wake, while the steady-state case exhibits an area of limited vorticity behind the hand. The

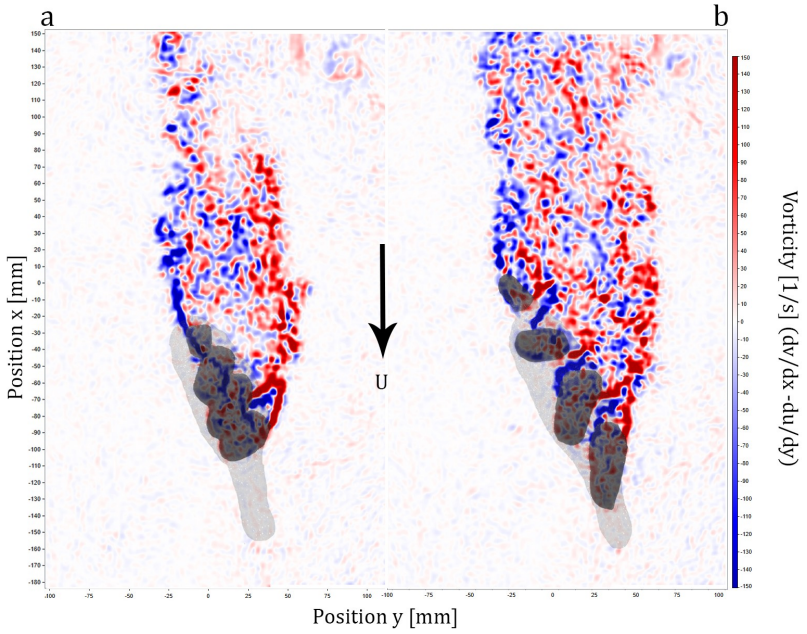

Figure 4.2.: PIV result for different hands at steady-state, with a) 0° hand and b) 20° hand. The velocity U is 600 mm s^{-1}

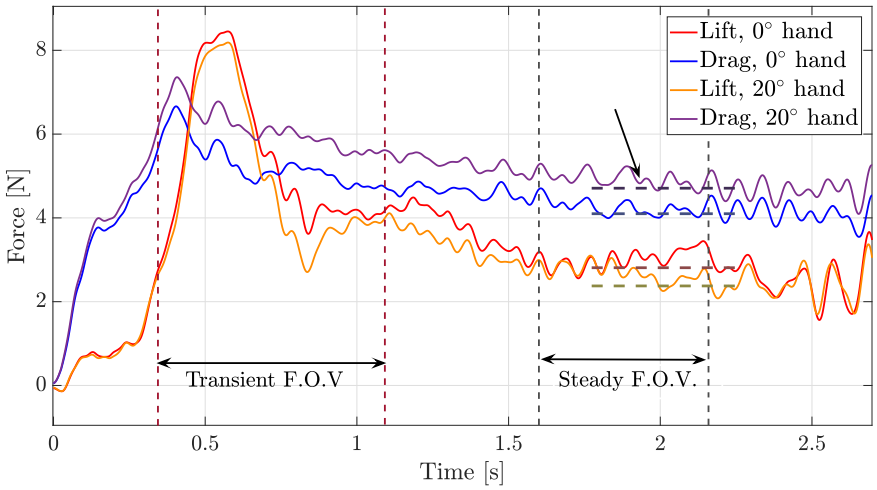

Figure 4.3.: Drag and lift result for 0 (blue, red) and 20° (purple, orange) hand, $\alpha = 30°$, Re $= 0.60 \cdot 10^5$. The figure shows both PIV field of views (vertical dotted lines) and the steady-state averaging window as is presented in Figure 3.4, with the mean drag and lift force value shown with horizontal dotted lines, based on Figure 3.8). The black arrow shows the instance presented in Figure 4.2.

concentrated wake leads to a lower pressure behind the hand, leading to a higher pressure

difference. This might be behind the increased lift and drag forces.

In the transient case, the vortex street visibly shifts more towards the left compared to the steady-state case. It is plausible that the vortex street results from a delayed stall, resembling Figure 1.5. This delay could explain the significant lift peak observed in Figure 4.2.

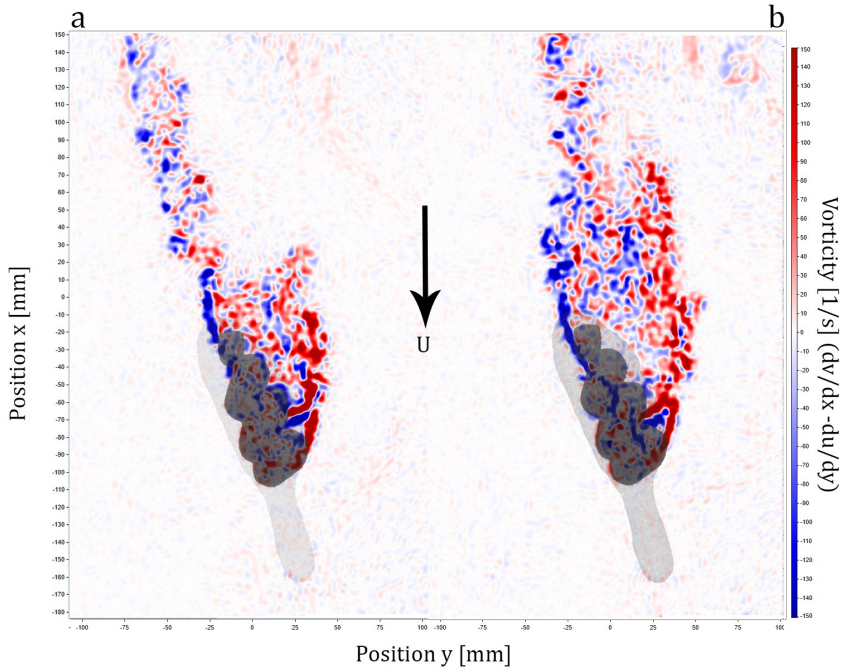

Figure 4.4.: PIV result for 0° hand, with a) result just after acceleration and b) the steady state result. The velocity U is 600 mm s^{-1}

4.3.3 Vorticity in far-wake

After the hand passes through the water, certain flow structures become visible. An instance of this is illustrated in Figure 4.5, featuring a 0° hand with angle $\alpha = 150°$ and a Reynolds number of $0.6 \cdot 10^5$. The black arrows in the figure indicate areas of high and low vorticity, which have an impact on the flow structure. The vortices are closely monitored in the images to determine the shedding time. It is observed that the positive circulation (red areas) is shed at a frequency between 6 and 9 Hz, while the negative vortices are shed at frequencies of about 8 to 9 Hz. The medium-frequency lift force oscillations from chapter 3 for this particular case are between 11 and 15 Hz, corresponding to a spacing of 54 to 40 mm. These are not visible in the flow field, indicating that additional smaller vortices or other three-dimensional effects are present.

A shedding frequency of 2 Hz is observed for the hand-shaped ellipse in chapter 2. This corresponds to a shedding distance of 300 mm, which is almost out of the investigated frame. However, some hints can be perceived in Figure 4.5; at the top and bottom, the vorticity is shifted to the left, while the middle part is directed more to the right. This seems to indicate a larger scale shedding at about the same frequency.

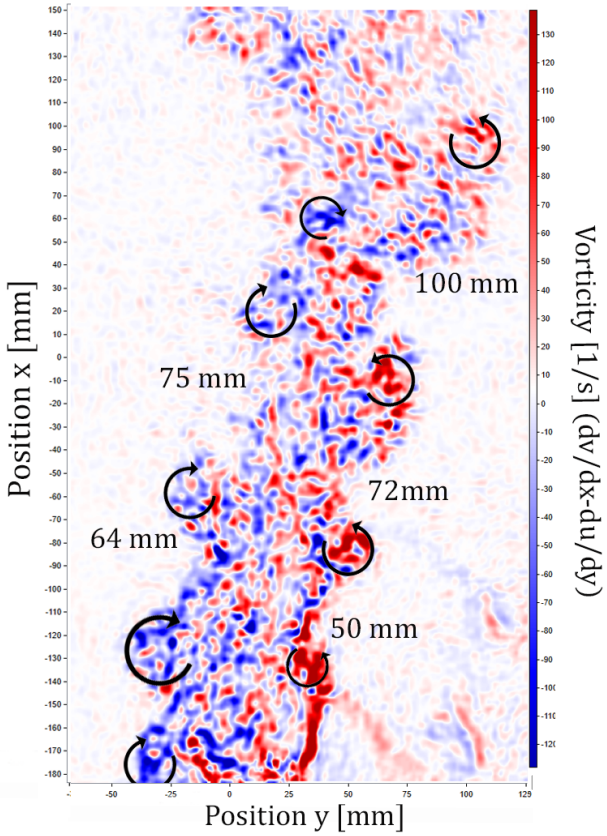

Figure 4.5.: The wake when the hand is out of the field of view, $\alpha = 150°, U = 600\,\mathrm{mm\,s^{-1}}$

4.3.4 Circulation

This section compares the forces obtained from the observed flow field to the sensor's force result. To retrieve the circulation Γ, the vorticity ω_z is integrated over the surface,

$$\Gamma = \iint_S \omega_z dS, \tag{4.4}$$

with S being the surface. The circulation is used to calculate the lift in the $x-y$ plane, using the Kutta-Joukowski equation, $F_L = \rho U \Gamma$. A rectangular mask is placed around the hand to accurately compare the force result, allowing only a portion of the upstream vorticity to affect the lift measurement. The mask translated along the x-axis, with constant velocity, U.

As seen in Figure 4.4, there is a substantial presence of vorticity upstream of the hand. Clockwise or negative vorticity can be noticed near the hand, while counterclockwise vorticity is visible in its wake. This observation is also supported by the circulation plot depicted in Figure 4.7. As the masked hand comes into view, the vorticity is negative, while it becomes positive in the wake. The lift force's dependence on the wake is determined by the flow conditions and hand parameters, which are specific to each situation. This study assumes that the maximum distance where the wake would influence the lift is equivalent to one chord length of the hand, L_H, counted from the last finger. The mask's width is chosen so it does not interfere with the wake, and due to low vorticity in the downstream area, this length is taken at random. Four elliptical shapes are used and interpolated between three instances

to mask the fingers. This creates a continuous and translated deforming mask that can adjust to the different finger shapes caused by the warped image. These ellipses are moved with a constant velocity, U. The mask is shown in Figure 4.6.

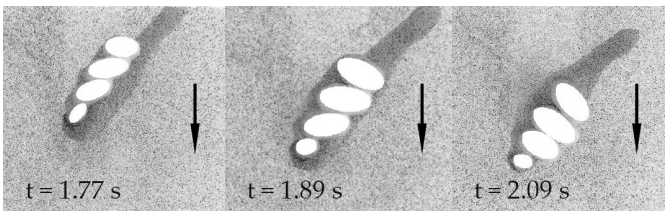

Figure 4.6.: Translated mask in three instances, for a 0° hand at an angle of attack, α of 150°.

The two-dimensional lift result is assumed constant over the whole arm and multiplied by the submerged length to compare to the three-dimensional force result. In the comparison shown in Figure 4.7, the circulation lift is compared to the force result for a steady-state experiment with $\alpha = 30°$ and a velocity of $U = 0.6\,\mathrm{m\,s^{-1}}$. Both signals display frequency variations of a similar order of magnitude, although they seem slightly out of phase. Altering the length of the upstream mask leads to some change in the detected circulation, which suggests a notable correlation between the size of the wake and the lift force. The result can be compared to the simulated ellipse from chapter 2; for this particular numerical simulation, a lift force of 3.4 N was found. In summary, it can be stated that the combination of the current 2D plane and the chosen wake matches the lift well to the measured lift force. This may not be correct for all cases.

In a similar manner, the circulation from other experiments is compared to the relevant measured lift force. The difference is shown in Figure 4.8, with the blue bars equalling the measured lift force and the orange bars the lift force from circulation.

A notable contrast in the observed circulation and measured forces is evident when accelerating at an angle of $\alpha = 30°$; a plot of this case is presented in appendix E. Two possible explanations for this discrepancy have been proposed: firstly, the starting vortex, which is located relatively close and outside the frame, may be affecting the outcome. Secondly, it is possible that the illuminated plane is not fully representative of the entire arm during this phase.

4.4 Conclusion

PIV Experiments are conducted on some interesting cases from chapter 3. There is a noticeable difference when comparing the wakes produced by a 0° and 20° hand. The 20° hand creates a wider and more turbulent wake, with additional jets, potentially leading to increased drag. The difference in lift observed is likely due to a decrease in the resulting pressure over the hand due to the wide-spread fingers. The steady-state and transient cases show a significant difference in the vorticity fields; the transient case shows a more concentrated wake near the hand and a vortex street moving to the left; this wake leads to a lower pressure behind the hand and a subsequent higher pressure difference, this pressure difference might be behind the increased drag and lift peaks. Delayed stall is possibly another reason behind the perceived lift peak, where the vortex street is similar to Figure 1.5.

The perceived medium-frequency oscillations are not observed as shedded vortices in the current plane. As a result, smaller vortices or other out-of-plane effects must be the cause.

In most investigated cases, lift forces in the two-dimensional plane were comparable to

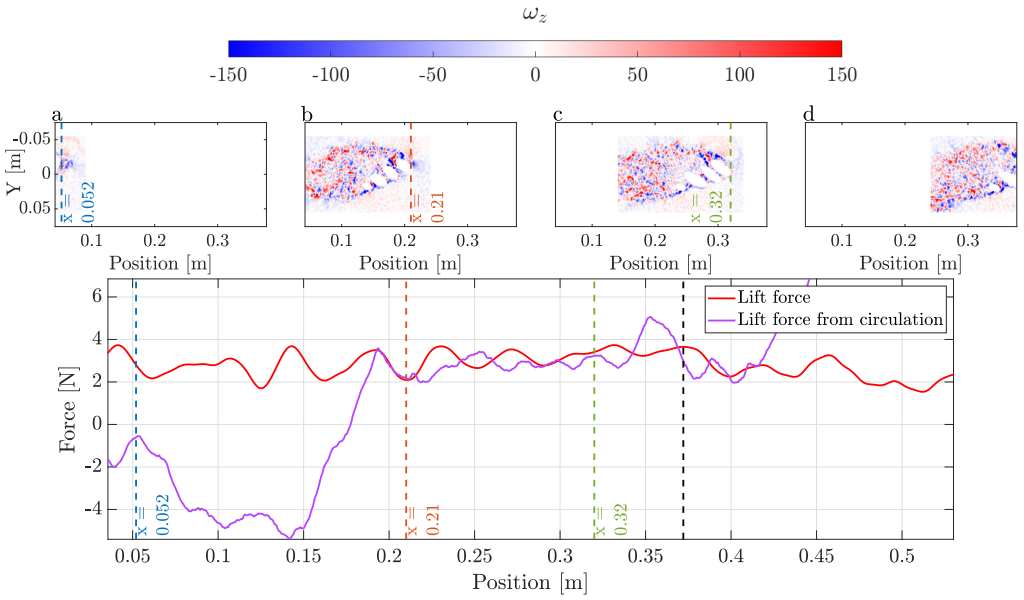

Figure 4.7.: Comparison of lift forces, with the response of the force sensor (red) and the force found via the circulation in the PIV plane (purple), to make a comparison, the 2D lift force is assumed evenly over the whole submerged arm. The hand and the wake are not always completely in the field of view (see figures a and d); in figure b, the non-masked wake is completely in range; this region is shown in the bottom plot (orange to black line).

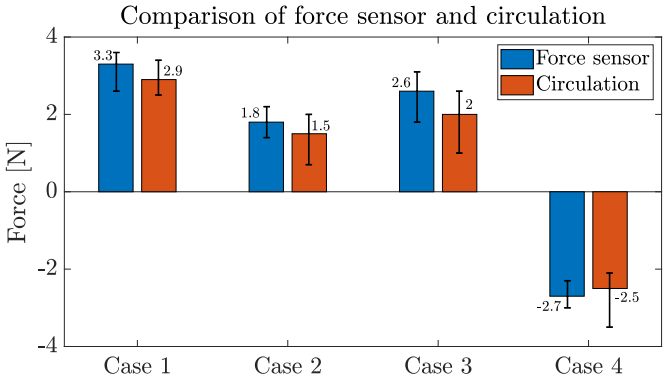

Figure 4.8.: Difference between measured steady-state circulation between the force sensor (blue, right) and the circulation (orange, left), for case 1: $V = 600\,\mathrm{mm\,s^{-1}}$, $\alpha = 30°$, 0° hand; Case 2: $V = 450\,\mathrm{mm\,s^{-1}}$, $\alpha = 30°$, 0° hand; Case 3: $V = 600\,\mathrm{mm\,s^{-1}}$, $\alpha = 30°$, 20° hand; Case 4: $V = 600\,\mathrm{mm\,s^{-1}}$, $\alpha = 150°$, 0° hand.

those measured by the force sensor. This may come as a surprise because the investigated plane has a higher lift coefficient than the arm (see chapter 2). The circulation was expected to generate a greater lift force than the force sensor once the plane's lift was normalized over the entire arm. This discrepancy might be due to the length of the chosen wake, which is

equivalent to the characteristic length scale of the hand. By increasing the wake length, a higher circulation is obtained; additional experiments should point out the relevant wake length.

5. Comparing different strokes

Extensive research on the drag and lift of swimming hands is conducted in chapters 3 and 4. However, the experiments are performed with a constant angle. A proper sculling stroke is a dynamic movement that involves various angles, which can lead to other relevant fluid phenomena. For example, Takagi et al. [2014b] investigated movements that imitated both strokes and discovered completely different mechanisms present. Examining the dynamic stroke is crucial to fully comprehend the mechanics of lift in front crawl swimming. This understanding can lead to discovering the key to reaching the fastest swimming speeds.

This chapter compares three simplified strokes: the straight stroke, the sculling stroke, where the hand follows the path, and the sculling stroke, where the hand's palm faces the direction of the swimming movement. The strokes will be analysed based on a variety of factors to provide insight into how to maximise propulsive forces and determine the most energy-efficient stroke.

5.1 Experimental setup

The experiments are conducted using the robot arm and water tank described in chapter 3. The water tank measures 2x0.57x0.5 in terms of length, width, and height. Two glass panels with a width of 0.1 m are glued at the top on both sides along the length to reinforce the tank. This imposes restrictions on the stroke width, which is further elaborated in the following section. The forces are defined identically to the ones shown in Figure 3.3.

5.2 Experimental methods

In this investigation, three types of strokes are compared. The first is a straight stroke, similar to previous trials. The other two are sculling strokes, which involves a sinusoidal movement and are inspired by experiments conducted by Sidelnik and Young [2006]. It is important to note that the sculling strokes are limited by the tank's size, specifically the glass reinforcements' width. A minimal distance of 0.05 meters is maintained between the arm and the glass reinforcements during the stroke to ensure a safe margin. As a result, the maximum amplitude A_s of the sinusoidal stroke is 0.075 meters, which, according to the findings of Sato and Hino [2002], is a 25 % reduction of a normal stroke width. The traversed path of the straight stroke measures 1.50 m in length, while the sinusoidal stroke is 1.555 m long, indicating a length increase of 3.7 %. A top view of the strokes is shown in Figure 5.1.

When it comes to sculling, there are two variations to consider. The first one involves the palm of the hand being directed in the same direction as the movement i.e. the palm of the hand always faces the direction of the drag, this is called the direction following (DF) stroke. The second variation involves the palm of the hand always being directed in the X-direction and is referred to as the constant angle (CA) stroke. The DF stroke is only conducted for the 20° hand, totalling a total of five unique experiments.

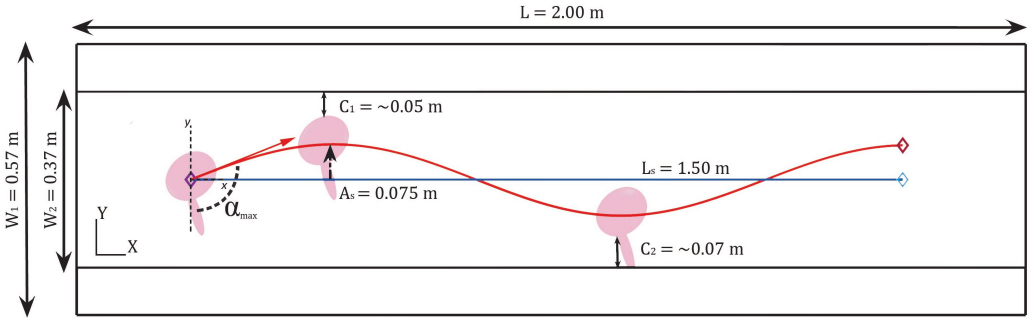

Figure 5.1.: Taken stroke path, with blue the straight stroke and in red the curved stroke. The maximum angle α varies between 69° and 111°. In the current figure, the hand palm is directed in the plus X-direction.

5.2.1 Kinematics

The arms are accelerated to an end velocity U_{end} of $0.6\,\mathrm{m\,s^{-1}}$. The accelerations vary due to the shape of the movement. Therefore, the analysis will focus on the steady-state phase, this phase is determined by analysing the resulting force responses.

5.3 Results and discussion

This section presents the experimental results. Initially, the force profile for each type of stroke is displayed. Then, we compare the resulting lift-to-drag ratio with previous experiments. Finally, the efficiencies obtained from each stroke are compared using the method described by Grift et al. [2021] for a rowing blade.

5.3.1 Force profile

In Figure 5.2, the found lift and drag forces for a 20° hand are plotted against time; due to the dynamic movement, the robot arm can move more joints, which results in higher acceleration and forces at the start. Nonetheless, the cases can be compared in the steady-state regime after some time. The Constant Angle (CA) stroke generates the most lift, which was expected. The other strokes have the hand palm always directed in the flow direction, generating almost no lift.

Due to the stroke movement, not all drag will be used as propulsion and not all lift equals the non-propulsive component. In Figure 5.3, the resulting propulsive and non-propulsive components are plotted. It is observed that the Direction Following (DF) stroke generates the most non-propulsive force.

5.3.2 Lift-to-drag ratio

The sculling strokes have a maximum angle deviation $|\alpha_{max}|$ of $\pm 21°$. The lift-to-drag ratio for the sculling movement with a constant angle is plotted against the corresponding angle, α and compared to the performed experiments from chapter 3, where Figure 3.11 shows the results plotted for the entire range of angles of attack.; the comparison is shown in Figure 5.4. Around $t = 0.40\,\mathrm{s}$, a larger L/D ratio is observed due to increased acceleration for the dynamic experiments. At $t = 0.80\,\mathrm{s}$, the ratio reaches a steady state, but in the dynamic case, a higher value is reached after the gradient of the angle of attack changes signs; this

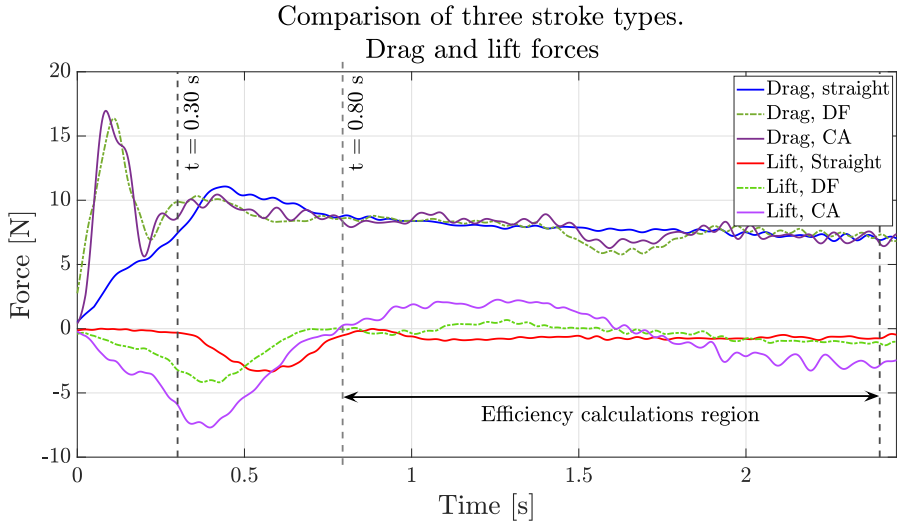

Figure 5.2.: Drag and lift forces against time for three investigated cases. The signal is filtered with a movmean filter with a window size of 500 for better readability.

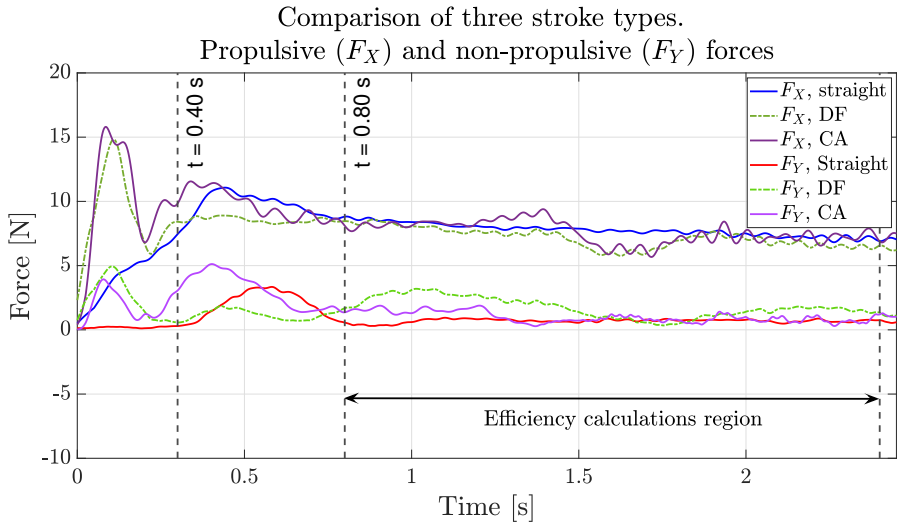

Figure 5.3.: Plot of propulsive (F_X) and non-propulisve ($|F_Y|$) forces against time for three investigated cases.

could be attributed to any dynamic effects, like wake capture. By $t = 1.71\,\text{s}$, both lines align perfectly. Overall, it can be concluded that no significant dynamic effect is observed in this experiment.

5.3.3 Energetic efficiencies

This paragraph follows the process proposed by Grift et al. [2021], which was utilised to gain insights on a rowing blade. The process solely focuses on the external power of the limbs exerted on the water and does not take into account any internal processes. When

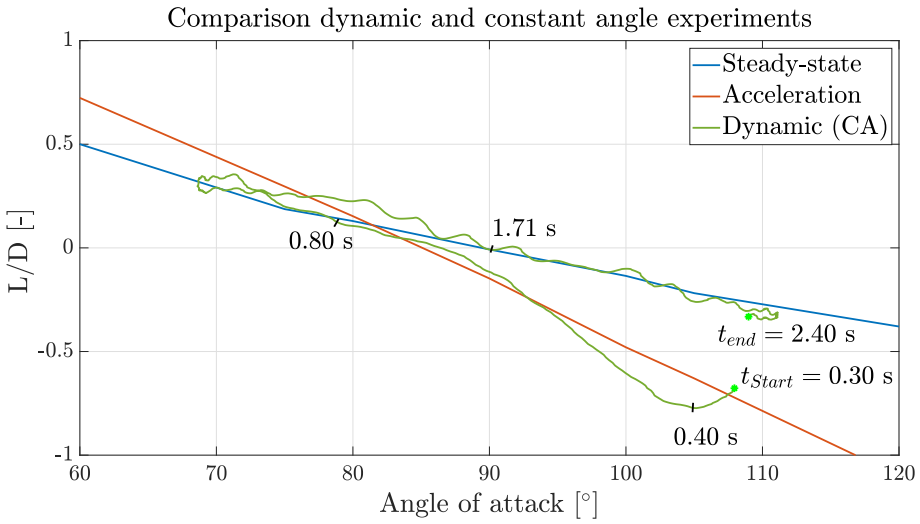

Figure 5.4.: Comparison of the Lift-to-Drag ratio of a dynamic sculling stroke (green) and experiments from chapter 3.

comparing stroke performance, it is important to only consider the steady-state portion due to differences in starting acceleration. When looking at Figure 5.2, the efficiencies of all strokes are compared over a distance of 1 m in the direction of propulsion (L_X). The measurement starts at $t_{start} = 0.80$ s and ends when the hand has moved a distance of one meter in the X-direction. Three different efficiencies are compared, the energetic efficiency η_E, the impulse efficiency η_J and the Froude efficiency, η_F. All three are described in the following section.

The propulsion generated during each stroke equals the total change in momentum, also known as the impulse vector $\mathbf{J}(t)$.

$$\mathbf{J}(t) = \int_{t_{start}}^{t_{end}} \mathbf{F}(t)dt. \tag{5.1}$$

The force vector, denoted by $\mathbf{F}(t)$, comprises two components: the propulsive component, F_X, and the non-propulsive component, F_Y. The instantaneous power P is defined as,

$$P(t) = \mathbf{F}(t) \cdot \mathbf{v}(t). \tag{5.2}$$

Then, the total energy spent on the water equals,

$$E = \int_{t_{tstart}}^{t_{tend}} P(t)dt. \tag{5.3}$$

The energetic efficiency is defined as,

$$\eta_E = \frac{J_x}{E}, \tag{5.4}$$

where the efficiency is not non-dimensionalised by the lack of a suitable reference velocity. Another approach is how much of the impulse is directed in the desired direction. This is

known as impulse efficiency,

$$\eta_J = \frac{J_x}{|\mathbf{J}|}. \tag{5.5}$$

The third approach is to compare the power in the desired direction to the total exerted power; it is defined as,

$$\eta_F = \frac{P_x}{P_{tot}}. \tag{5.6}$$

Energetic outcomes

The efficiency chart shown in Figure 5.5 compares the five investigated cases. Based on expectations, both straight cases are expected to have an impulse efficiency of approximately one. However, the 20° angle case has a slightly lower impulse efficiency due to a lift that is not exactly zero (as seen in Figure 5.2). This difference is also noticeable when examining Figure 3.10, where the ratio does not cross zero at an angle of 90°. Furthermore, the velocity in the Y-direction is zero, resulting in a Froude efficiency of one for both cases.

The curved pulls with a constant angle show slightly lower impulse efficiencies; the non-propulsive impulse in the Y-direction is generally quite low ($\sim 9-14\,\%$); this is also observed when looking at the Figure 5.3 by comparing the area under the dark purple and light purple graphs. The Froude efficiency falls between 96.2 % and 97.5 %, indicating that a significant portion of the exerted power is still directed in the propulsive direction. Additionally, the energetic efficiency is about 5 % higher than their straight-stroke counterparts because less energy is spent, and the difference in the propulsive impulse (J_x) does not make up for the difference. The found stroke length difference was 3.7 %, which means that the curved stroke decreases the energy expenditure of the swimmer by $\sim 1.3\,\%$.

The DF stroke shows the highest non-propulsive forces; this also comes through in the observed efficiencies. The Froude efficiency, in particular, is low, with a value of 0.935. This is mainly caused by the high drag force in the non-propulsive direction when moving near the maximum angle α_max.

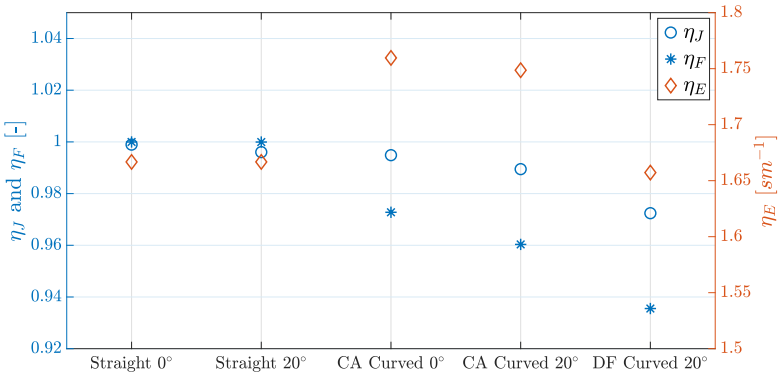

Figure 5.5.: Comparison of Impulse efficiency (η_J), Froude efficiency (η_F), and energetic efficiency (η_E) (right, different scale).

5.4 Conclusion

Two dynamic strokes, following a sinusoidal path in the tank are compared to their straight counterpart as investigated in chapter 3. The two strokes are either directed with the hand palm in the main swimming direction (CA) or in the local flow direction (DF). We focused on the steady-state region due to the different starting accelerations. The efficiency findings in Figure 5.5 demonstrate an incremental variation in the outcomes. While some deductions can be drawn, additional experiments with different stroke paths and velocities are necessary to obtain a more precise understanding and validate the findings.

The findings revealed that in the CA experiments, the majority of the drag and lift serve as propulsive forces (F_X), whereas, in the DF experiments, a greater proportion is used as non-propulsive forces (F_Y).

This can also be observed in the found energetic efficiencies, here the CA stroke constantly performed better compared to the DF stroke. Furthermore, the highest impulse, (η_I) and Froude (η_F) efficiency are seen for the straight stroke, indicating that this stroke is the most efficient for maximising propulsion, while the CA stroke scored the highest on the energetic efficiency, (η_E), indicating that it may be better suited for longer distances.

Figure 5.4 shows a clear correlation between the lift-to-drag ratio from Chapter 3 and the dynamic ratio for the CA stroke. This suggests that dynamic effects are not significant for the investigated strokes.

The experiments conducted in this chapter can serve as a starting point in gathering more understanding of the optimal stroke pattern. Both strokes are simplified, and the robot arm is able to nicely follow the kinematics and the required path. In order to improve future experiments, it is advisable to enlarge the tank and program the robot to adhere to the desired path, even for strokes with greater amplitudes and shorter wavelengths. Furthermore, PIV can be useful to visualise the flow field and to see if certain mechanics are observable.

6. Conclusion

Extensive research has been conducted on the force generation of front crawl propulsion, with a focus on lift. This research aims to settle a long-standing debate in the field regarding which stroke is optimal for front crawl propulsion: the curved or straight pull. Where the curved pull mixes drag and lift as forward propulsion, while the main stroke mainly uses drag. In Chapter 2, the forearm and hand model is divided into ten equally spaced sections along its length. Each cross-section is then approximated by a two-dimensional ellipse. Two analytical methods are implemented on the parameterised model to gather insight into the angle-dependent lift force. Due to the large amount of separation, the analytical models fail to correctly predict the lift coefficient, especially for large angles of attack and bluff bodies. Therefore, we can conclude that these methods can only qualitatively predict relevant lift forces in limited cases and at low angles of attack.

On the simplified model, numerical simulations are performed. Results show forces comparable in magnitude to literature when performing the simulations in a pseudo-transient steady-state. The numerical simulations differ significantly to the analytical methods.

Experiments with a new robot arm are performed in the following chapters, where chapter 3 focuses on the lift and drag of two identical hands with different finger spreading under various angles of attack. A steady-state region is formulated for all experiments, while an unsteady or transient region is observed after the impulsive start. Steady-state results, presented in Figure 2.9 show a higher lift coefficient for a hand with closed fingers, especially at high and low angles of attack. At an angle of attack of $> 90^\circ$ a higher drag coefficient is observed for the 0° hand, which is in correspondence with literature, while at lower angles of attack, the hand with a 20° finger spread shows a higher drag coefficient. Generally, the lift is lower than the drag coefficient for the steady-state case, which is graphically presented in Figure 3.10. A maximum ratio of 0.75 could be found for the 0° hand, while the maximum of the 20° hand is around 0.6.
A lift peak could be observed after the start, which was especially significant for high and low angles of attack. In Figure 3.11, the resulting lift-to-drag ratio is presented, showing a maximum ratio of 1.54 and -1.68 at low and high angles of attack. As these regions are considered the only places where lift forces dominate, these regions are further investigated, making use of PIV.

It is suggested that different experimental setups should be used for conducting experiments of this nature. The results obtained from the steady-state window were found to be subject to large uncertainties due to their limited size. Furthermore, due to the exceeded blockage ratio a correction model is used, which is only validated on a single angle of attack. Moreover, the oscillations experienced by the robot arm have the potential to obscure other fluid mechanisms. To reduce uncertainty, conducting the experiments again in a water or wind tunnel is recommended. Alternatively, a larger water tank and a smaller hand model can be used.

To conduct a more in-depth analysis of the lift force, we examined the flow field surrounding two cases where the lift was especially prevalent. The results revealed a broader and more turbulent wake for the 20° hand, which explains the higher drag force shown in Figure 4.2. The gaps between the fingers cause a decrease in pressure differential, which explains the

lower lift force. In the transient case, the wake moves to the left and creates lower pressure behind the hand, leading to an observed lift peak similar to a delayed stall. Based on the circulation method, the lift forces calculated appear to be comparable in strength to the actual measured forces.

Considering that the experiments of chapter 3 are performed at a constant angle of attack and that an S-stroke's angle is non-constant, two sinusoidal strokes are investigated. The results reveal that the lift-to-drag ratio is not significantly affected by a dynamic stroke. Furthermore, it is established that the straight stroke is the most effective for maximizing propulsion. On the other hand, a sinusoidal stroke with the hand palm directed towards the main swimming direction shows higher energy expenditure efficiency, making it a feasible option for longer distances.

A. Blockage ratio

A.1 Extended Maskell III method

The extended Maskell method developed by Hackett and Cooper [2001] is described in the following section. The blockage factor is calculated via,

$$\theta = 0.96 + 1.94 \exp^{-0.12 * h_m / w_m}, \tag{A.1}$$

with h_m the height of the object and w_m the width.

$$x = \theta * (\frac{A_p}{C_{dt}}), \tag{A.2}$$

with C_{dt} the test section area (HxW)

The drag increment due to wake distortion ΔC_{DM} is calculated following,

$$\Delta C_{DM} = C_D [\frac{1}{1+x} + \frac{1-\sqrt{1+4x}}{2x}]. \tag{A.3}$$

The Maskell corrected drag coefficient C_{DcM} is calculated via,

$$C_{DcM} - \Delta C_{DM} = \frac{-1+\sqrt{1+C_D x}}{2x} \tag{A.4}$$

$$\frac{q_c}{q} = 1 + x C_D - \Delta C_{DM}, \tag{A.5}$$

with q_c the corrected dynamic pressure and q the uncorrected.

The corrected drag coefficient $C_{D,c}$ is then calculated via,

$$C_{D,c} = \frac{C_{Duw}}{1 + x(C_{DcM} - \Delta C_{DM}} + \Delta C_{DM} \tag{A.6}$$

The lift coefficient can be corrected via,

$$\Delta C_{LM} = \frac{\Delta C_{DM}}{\tan \alpha} \qquad C_{L,c} = \frac{C_L}{qc/q} + \Delta C_{LM}. \tag{A.7}$$

A.2 Thom and Herriot's correction method

This correction method starts by correcting the dynamic pressure,

$$\frac{q_c}{q} = \left[1 + T\left(\frac{V_m}{A_w^{3/2}}\right) + 1/4 C_D \frac{A_p}{A_w}\right], \tag{A.8}$$

with T the water tank shape factor $T = 0.36\,(w_t/h_t + h_t/w_t)$. V_m is the volume of the object, while A_w is the cross-section of the water tank. The following equations are then used to correct for the drag and lift coefficient,

$$\begin{aligned} C_{D,c} &= \frac{C_D - T\left(\frac{V_m}{A_w^{3/2}}\right) C_D}{q_c/q} \\ C_{L,c} &= \frac{C_L - T\left(\frac{V_m}{A_w^{3/2}}\right) C_L}{q_c/q}. \end{aligned} \tag{A.9}$$

B. Velocity potential derivation

B.1 Derivation

B.1.1 Complex potential & velocity

The complex potential $F(z)$ is an analytical function, which is expressed with ϕ and ψ as follows,

$$F(z) = \phi(x,y) + i\psi(x,y), \tag{B.1}$$

with $z = x + iy$, for every function $F(z)$, the real part is a velocity potential and for the imaginary part, a stream function. The complex velocity, $W(z)$, is the derivative of the complex potential.

B.1.2 Elementary flows

The flow around a cylinder can be expressed by a uniform flow, a doublet and rotation. The uniform flow is one of the simplest building blocks and is defined with a flow angle α as,

$$\begin{aligned} F(z) &= Ue^{i\alpha}z \\ W(z) &= u - iv = U\cos\alpha - iU\sin\alpha. \end{aligned} \tag{B.2}$$

The rotation is defined as a vortex around a single point and is defined as,

$$\begin{aligned} F(z) &= i\frac{\Gamma}{2\pi}\ln z \\ W(z) &= i\frac{\Gamma}{2\pi}\frac{1}{z}. \end{aligned} \tag{B.3}$$

A source at point z_0 and strength m is defined as,

$$\begin{aligned} F(z) &= \frac{m}{2\pi}\ln z - z_0 \\ W(z) &= \frac{m}{2\pi z}. \end{aligned} \tag{B.4}$$

A sink is the opposite of a source, and the m is replaced by $-m$. A doublet is a combination of a very strong source and a very strong sink which are very close together, the distance $z_{source} = -z_{sink} \longrightarrow 0$ and $m \longrightarrow \infty$, delivers a complex potential of,

$$\begin{aligned} F(z) &= \frac{\mu}{z} \\ W(z) &= -\frac{\mu}{z^2}, \end{aligned} \tag{B.5}$$

where μ is a constant.

B.1.3 Complex potential and complex velocity result

First, a cylinder with a varying incoming flow can be defined with a uniform flow at an angle α and a doublet,

$$F(z) = Uze^{-i\alpha} + \frac{\mu}{z}e^{i\alpha} \tag{B.6}$$

The flow around the circle, where $R = a$, needs to be a streamline, so $\psi = 0$, for a cylinder, $z = ae^{i\theta}$, thus,

$$\begin{aligned} F(z) &= Uae^{i\theta}e^{-i\alpha} + \frac{\mu}{a}e^{-i\theta}e^{i\alpha} \\ &= (Uae^{-i\alpha} + \frac{\mu}{a}e^{i\alpha})\cos\theta + i(Uae^{-i\alpha} - \frac{\mu}{a}e^{i\alpha})\sin\theta, \end{aligned} \tag{B.7}$$

The streamlines are defined by the imaginary part and should equal zero, so

$$\psi = (Uae^{-i\alpha} - \frac{\mu}{a}e^{i\alpha})\sin\theta, \tag{B.8}$$

is zero for $\mu = Ua^2$.

The flow past a cylinder with circulation can then be defined as,

$$F(z) = U(ze^{-i\alpha} + \frac{a^2}{z}e^{i\alpha}) + i\frac{\Gamma}{2\pi}\ln z + c, \tag{B.9}$$

where c is a constant that ensures the addition of the vortex does not influence $\psi = 0$ at $R = a$, the value of this constant is $c = -\frac{i\Gamma}{2\pi}\ln a$, giving the complex potential and velocity,

$$\begin{aligned} F(z) &= U(ze^{-i\alpha} + \frac{a^2}{z}e^{i\alpha}) + i\frac{\Gamma}{2\pi}\ln\frac{z}{a} \\ W(z) &= U(e^{-i\alpha} - \frac{a^2}{z^2}e^{i\alpha}) + i\frac{\Gamma}{2\pi}\frac{1}{z} \\ W(z) &= U(e^{-i\alpha} - \frac{a^2}{r^2}e^{i\alpha}e^{-2i\theta}) + i\frac{\Gamma}{2\pi}\frac{1}{r}e^{-i\theta} \\ W(z) &= (U(e^{-i\alpha}e^{i\theta} - \frac{a^2}{r^2}e^{i\alpha}e^{-i\theta}) + i\frac{\Gamma}{2\pi r})e^{-i\theta} \\ W(z) &= [(U(e^{-i\alpha} - \frac{a^2}{r^2}e^{i\alpha})\cos\theta + i(U(e^{-i\alpha} + \frac{a^2}{r^2}e^{i\alpha})\sin\theta + \frac{\Gamma}{2\pi r})]e^{-i\theta}. \end{aligned} \tag{B.10}$$

The velocity components in cylindrical coordinates u_r and u_θ are then equivalent to the real and imaginary part of the complex velocity,

$$\begin{aligned} u_r &= U(1 - \frac{a^2}{r^2}) \cos(\theta - \alpha) \\ u_\theta &= -U(1 + \frac{a^2}{r^2}) \sin(\theta - \alpha) - \frac{\Gamma}{2\pi r}, \end{aligned} \tag{B.11}$$

On the surface of the cylinder, $r = a$, the velocity function u_r is always zero, the velocity u_θ is zero at the stagnation point,

$$\begin{aligned} u_r &= 0 \\ -2U \sin(\theta - \alpha) &= \frac{\Gamma}{2\pi a} \\ \theta - \alpha &= -\arcsin \frac{\Gamma}{4U\pi a}, \end{aligned} \tag{B.12}$$

The ellipse's lift and lift force coefficient are then calculated via the Kutta-Joukowski theorem $L = \rho \Gamma U$;

$$\begin{aligned} F_L &= 4\rho U^2 \pi a \sin\alpha \\ C_L &= \frac{F_L}{0.5\rho U^2 2a_1} = 4\pi \frac{a}{a_1} \sin\alpha, \end{aligned} \tag{B.13}$$

For an ellipse with semi-major axis $a_1 = a + \frac{\xi^2}{a}$, and semi-minor axis $a_2 = a - \frac{\xi^2}{a}$, definition of eccentricity

$$\beta = \frac{a_1 - a_2}{a_1 + a_2} = \frac{\xi^2}{a^2} \tag{B.14}$$

,

rewriting β in the form $\frac{a}{a_1}$ and inserting into equation B.13 gives us the complete equation for the lift coefficient,

$$C_L = 4\pi \frac{1}{1 + \beta} \sin\alpha \tag{B.15}$$

B.2 Comparison reference case, analytical result and JavaFoil

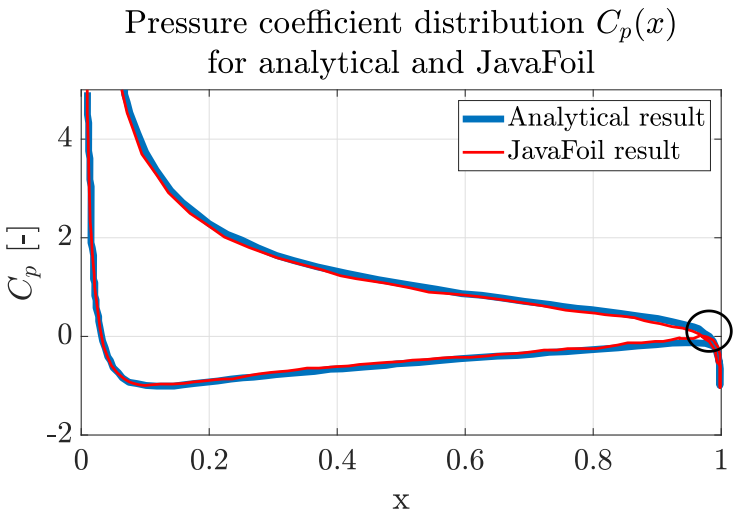

Figure B.1.: Inviscid $C_P(x)$ comparison of analytical (potential flow) and JavaFoil (advanced panel method) methods. The ellipse presented has an aspect ratio of eight, and the stream angle is 20°. The results match, although the results differ at the trailing edge.

C. CFD

C.1 2D simulations

The equations for the SST $k-\omega$ turbulence model

$$\frac{\partial(\rho k)}{\partial t}+\frac{\partial(\rho u_j k)}{\partial x_j}=\frac{\partial}{\partial x_j}\left[(\mu+\sigma_k\mu_t)\frac{\partial k}{\partial x_j}\right]+P_k-\beta^*\rho\omega k+\frac{\partial}{\partial x_j}\left[\rho(\nu+\sigma_{\nu 2}\nu_t)\frac{\partial k}{\partial x_j}\right] \tag{C.1}$$

Turbulent dissipation rate equation (ω in the equation):

$$\frac{\partial(\rho\omega)}{\partial t}+\frac{\partial(\rho u_j\omega)}{\partial x_j}=\frac{\partial}{\partial x_j}\left[(\mu+\sigma_\omega\mu_t)\frac{\partial\omega}{\partial x_j}\right]+\frac{\gamma}{\nu_t}\left[\left(\frac{\partial\omega}{\partial x_k}\right)^2+\left(\frac{\partial\omega}{\partial x_k}\right)^2\right]-\beta\rho\omega^2+\sigma_{\omega 2}\frac{\partial}{\partial x_j}\left[\rho(\nu+\sigma_{\nu 2}\nu_t)\frac{\partial\omega}{\partial x_j}\right], \tag{C.2}$$

with σ_k and σ_ω, the turbulent Prandtl number ratios, β^*, the turbulent Prandtl number for k, P_k, the turbulent production term for k. β, denotes the turbulent Prandtl number for ω and γ, a coefficient for the dissipation rate equation. $\sigma_{\nu 2}$, $\sigma_{\omega 2}$ are additional constants.

C.2 Mesh construction

In the wake and close to the ellipse, large gradients in the flow can be expected, resulting in smaller grid sizes. Separation occurs at the boundary between the ellipse and the fluid, significantly impacting the found drag and lift forces. Therefore a higher resolution close to the boundary is preferred; twenty inflation layers with a smooth transition and growth rate of 1.2 are constructed around the ellipse to solve the flow accurately.

Around the ellipses the grid size is 0.05 mm. A circle with a radius of 200 mm is constructed around the ellipse, and the grid size is incrementally varied to a global grid size set at 15 mm.

C.2.1 Mesh validation

To validate the mesh, three parameters are considered: the wall $y+$, the orthogonality and the aspect ratio of the cells. First, the wall $y+$ is validated. In a turbulent flow, there is a very high change in gradients near the wall. Therefore, it is important that the first cell near the wall has a sufficient cell size. The wall $y+$ is a non-dimensional distance related to the Reynolds number and signifies the ratio between the turbulent and laminar influences in a cell Salim and Cheah [2009]. The distance $y+$ can be divided into 3 subsections; first, the log layer, where the inertia effect is dominant ($y+ > 30$), followed by the buffer layer ($5 < y+ < 30$) where both viscous and inertia forces rule and lastly, the viscous sublayer ($y+ < 5$) where viscous forces are dominant. A wall distance greater than $y+ > 30$ or smaller

than $y+ < 5$ is preferred for an accurate solution. The wall $y+$ is defined as,

$$y+ = \frac{yu_\tau}{\nu}, \tag{C.3}$$

with the friction factor u_τ and the kinematic viscosity ν. For all meshes, the wall y+ is accepted as it lies sufficiently within the viscous sublayer, and further refinement would lead to longer calculation times. Figure C.1 plots an example profile of the wall $y+$.

The orthogonal quality and aspect ratio is checked and improved if the values are deemed too low. In appendix C, a table with relevant meshing validation parameters is provided.

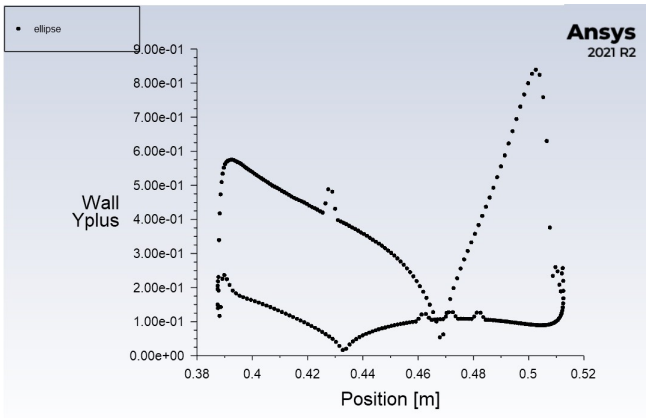

Figure C.1.: Wall $y+$, for ellipse eight, the velocity is directed perpendicular to the semi-major axis a_1. The maximum value is well under the viscous limit of 5.

For each face, the orthogonal quality is a value calculated by normalizing the dot product of the area vector of the face and a vector from the cell's centroid to the centroid of the face. The minimum orthogonal quality is the lowest dot product among all faces between the area vector of the face and a vector from the cell's centroid to the centroid of the face, and it should be above 0.15, with the average significantly higher. The aspect ratio measures the degree of stretching of a cell, and it should be kept below ten. Although the tiny cells along the ellipse in the current simulation have very high aspect ratios, they are kept as is because they are important for the wall $y+$.

Table C.1.: Minimal orthogonal quality and max aspect ratio of each configuration mesh.

Configuration	Min. orthogonal quality	Max. aspect ratio
Ellipse 1	0.438	5.879
Ellipse 4	0.487	5.756
Ellipse 7	0.499	5.646
Ellipse 9	0.354	5.817

D. Corrected Lift-to-Drag ratio using the Maskell III method

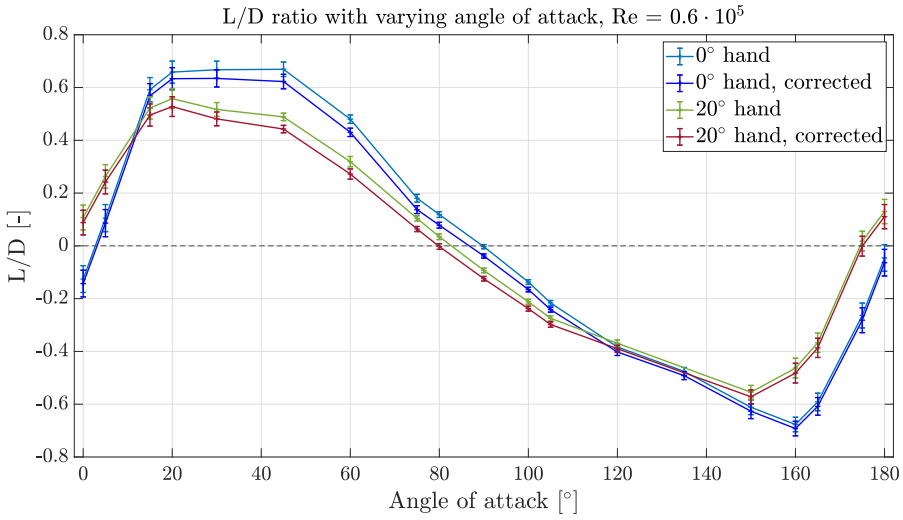

Figure D.1.: L/D ratio for Re = $0.60 \cdot 10^5$. The Lift-to-Drag ratio has been corrected, and there is only a slight difference between the corrected and uncorrected results.

E. PIV

E.1 PIV settings

Table E.1.: PIV settings used in experiments.

PIV parameters	
Calibration	6.01 pixels/mm
Initial interrogation window	32x32 pixels
Final interrogation window	16x16 pixels
Overlap	50 %
Field of view	335.21x335.21 mm
Sheet thickness	1.5 mm
Window spacing	1.32 mm
Camera frequency	1.28 kHz
Images per experiment	3124 images
Particle diameter, d_p	$53 - 63\,\mu m$
Particle density, ρ_p	$0.985 - 1.005\,g\,cm^{-3}$

Table E.2.: The performed experiments with two different states, angles, and velocities. This, in turn, gives sixteen unique experiments.

Re\Setup	0°				20°			
	Steady-state		Transient		Steady-state		Transient	
	30	150	30	150	30	150	30	150
0.6*10^5	x	x	x	x	x	x	x	x
0.6*10^5	x	x	x	x	x	x	x	x

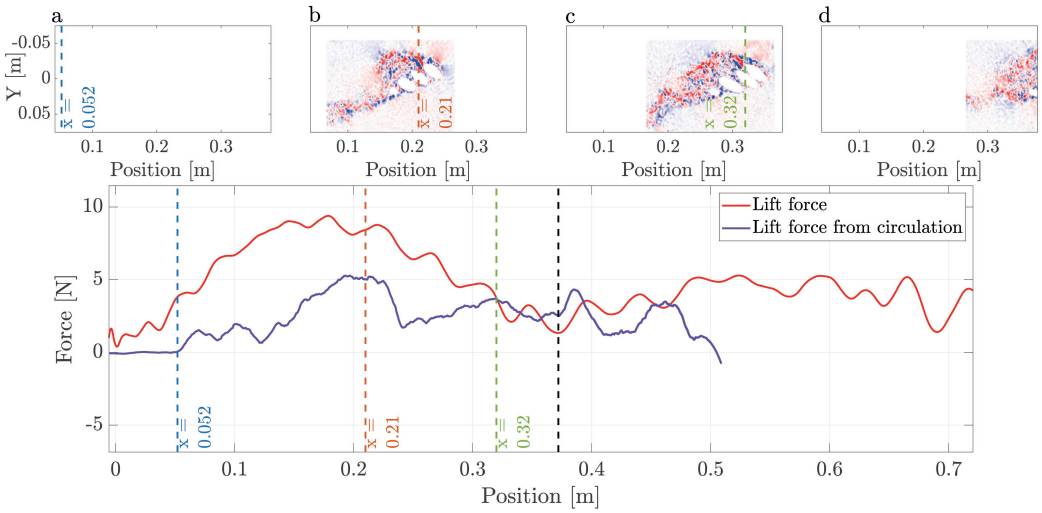

Figure E.1.: Circulation and force response of transient case, the lift peak is seen for both plots, but not comparable in magnitude, also a steep decline is seen in the circulation around $x = 0.23\,\mathrm{m}$. The wake is slightly extended, as this drastically improved the result.

Bibliography

Adrian, R. and Westerweel, J. (2011). *Particle Image Velocimetry*. Cambridge University Press.

Bazuin, R. (2018). The effects of hand configuration on propulsive forces in swimming. *Delft University of Technology*.

Berger, M. A. (1999). Determining propulsive force in front crawl swimming: A comparison of two methods. *Journal of Sports Sciences*, 17(2):97–105.

Bihan, E. L. (2020). Experimental investigation of drag propulsion on an accelerating hand for various finger spreading in human swimming. *Delft University of Technology*.

Bilinauskaite, M., Mantha, V. R., Rouboa, A. I., Ziliukas, P., and Silva, A. J. (2013). Computational fluid dynamics study of swimmer's hand velocity, orientation, and shape: Contributions to hydrodynamics. *BioMed Research International*, 2013:1–14.

Bin-Khalid, U. and Suda, J. M. (2020). Comparative study of aerodynamic blockagecorrection methods for swimmer's hand model.

Brennen, C. (1982). *A Review of Added Mass and Fluid Inertial Forces*. Chief of Naval Material, Port Hueneme, CA.

Chollet, Chalies, and Chatard (2000). A new index of coordination for the crawl: Description and usefulness. *International Journal of Sports Medicine*, 21(1):54–59.

Cohen, R. C. Z., Cleary, P. W., Mason, B. R., and Pease, D. L. (2017). Forces during front crawl swimming at different stroke rates. *Sports Engineering*, 21(1):63–73.

Counsilman, J. E. (1968). *The Science of Swimming*. Prentice-Hall.

Dickinson, M. H. (1996). Unsteady mechanisms of force generation in aquatic and aerial locomotion. *American Zoologist*, 36(6):537–554.

Grift, E., Tummers, M., and Westerweel, J. (2021). Hydrodynamics of rowing propulsion. *Journal of Fluid Mechanics*, 918.

Grift, E. J., Vijayaragavan, N. B., Tummers, M. J., and Westerweel, J. (2019). Drag force on an accelerating submerged plate. *Journal of Fluid Mechanics*, 866:369–398.

Hackett, J. E. and Cooper, K. R. (2001). Extensions to maskell's theory for blockage effects on bluff bodies in a closed wind tunnel. *The Aeronautical Journal*, 105(1050):409–418.

Kudo, S., Vennell, R., and Wilson, B. (2013). The effect of unsteady flow due to acceleration on hydrodynamic forces acting on the hand in swimming. *Journal of Biomechanics*, 46(10):1697–1704.

Kudo, S., Vennell, R., Wilson, B., Waddell, N., and Sato, Y. (2008). Influence of surface penetration on measured fluid force on a hand model. *Journal of Biomechanics*, 41(16):3502–3505.

Kundu, P. K., Cohen, I. M., and Dowling, D. R. (2016). *Fluid Mechanics*. Elsevier.

Mahasidha R. Birajdar, S. A. K. (2015). Effect of leading edge radius and blending distance from leading edge on the aerodynamic performance of small wind turbine blade airfoils. *Science Publishing Group*.

Marinho, D., Barbosa, T., Rouboa, A., and Silva, A. (2011). The hydrodynamic study of the swimming gliding: a two-dimensional computational fluid dynamics (CFD) analysis. *Journal of Human Kinetics*, 29(2011):49–57.

Marinho, D. A., Barbosa, T. M., Reis, V. M., Kjendlie, P. L., Alves, F. B., Vilas-Boas, J. P., Machado, L., Silva, A. J., and Rouboa, A. I. (2010). Swimming propulsion forces are enhanced by a small finger spread. *Journal of Applied Biomechanics*, 26(1):87–92.

Marinho, D. A., Rouboa, A. I., Alves, F. B., Vilas-Boas, J. P., Machado, L., Reis, V. M., and Silva, A. J. (2009). Hydrodynamic analysis of different thumb positions in swimming. *Journal of sports science & medicine*, 8:58–66.

Maskell, E. C. (1963). A theory of the blockage effects on bluff bodies and stalled wings in a closed wind tunnel. *Aeronautical Research Council London*.

Matsuuchi, K., Miwa, T., Nomura, T., Sakakibara, J., Shintani, H., and Ungerechts, B. (2009). Unsteady flow field around a human hand and propulsive force in swimming. *Journal of Biomechanics*, 42(1):42–47.

Matsuuchi, K. and Muramatsu, Y. (2011). Investigation of the unsteady mechanism in the generation of propulsive force while swimming using a synchronized flow visualization and motion analysis system. In *Biomechanics in Applications*. InTech.

Minetti, A. E., Machtsiras, G., and Masters, J. C. (2009). The optimum finger spacing in human swimming. *Journal of Biomechanics*, 42(13):2188–2190.

Pai, Y.-C. and Hay, J. G. (1988). A hydrodynamic study of the oscillation motion in swimming. *International Journal of Sport Biomechanics*, 4(1):21–37.

Rouboa, A., Silva, A., Leal, L., Rocha, J., and Alves, F. (2006). The effect of swimmer's hand/-forearm acceleration on propulsive forces generation using computational fluid dynamics. *Journal of Biomechanics*, 39(7):1239–1248.

Salim, S. M. and Cheah, S. (2009). Wall y+ strategy for dealing with wall-bounded turbulent flows. volume 2175.

Samson, M., Bernard, A., Monnet, T., Lacouture, P., and David, L. (2017). Unsteady computational fluid dynamics in front crawl swimming. *Computer Methods in Biomechanics and Biomedical Engineering*, 20(7):783–793.

Sarpkaya, T. (1986). Force on a circular cylinder in viscous oscillatory flow at low keulegan—carpenter numbers. *Journal of Fluid Mechanics*, 165(-1):61.

Sato, Y. and Hino, T. (2002). Estimation of thrust of swimmer's hand using cfd. In *Conference: 2nd International Symposium on Aqua Bio-Mechanisms*.

Sato, Y. and Hino, T. (2013). A computational fluid dynamics analysis of hydrodynamic force acting on a swimmer's hand in a swimming competition. *Journal of sports science & medicine*, 12:679–689.

Schleihauf, R. E. (1979). A hydrodynamic analysis of swimming propulsion. *Swimming III. Proceedings of the Third International Symposium of Biomechanics in Swimming, University of Alberta, Edmonton, Canada*, pages 70–109.

Sidelnik, N. O. and Young, B. W. (2006). Optimising the freestyle swimming stroke: the effect of finger spread. *Sports Engineering*, 9(3):129–135.

Soh, J. and Sanders, R. (2019). The clues are in the flow: how swim propulsion should be interpreted. *Sports Biomechanics*, 20(7):798–814.

Takagi, H., Nakashima, M., Ozaki, T., and Matsuuchi, K. (2013). Unsteady hydrodynamic forces acting on a robotic hand and its flow field. *Journal of Biomechanics*, 46(11):1825–1832.

Takagi, H., Nakashima, M., Ozaki, T., and Matsuuchi, K. (2014a). Unsteady hydrodynamic forces acting on a robotic arm and its flow field: Application to the crawl stroke. *Journal of Biomechanics*, 47(6):1401–1408.

Takagi, H., Nakashima, M., Sato, Y., Matsuuchi, K., and Sanders, R. H. (2015). Numerical and experimental investigations of human swimming motions. *Journal of Sports Sciences*, 34(16):1564–1580.

Takagi, H., Shimada, S., Miwa, T., Kudo, S., Sanders, R., and Matsuuchi, K. (2014b). Unsteady hydrodynamic forces acting on a hand and its flow field during sculling motion. *Human Movement Science*, 38:133–142.

Takagi, H., Shimizu, Y., Kurashima, A., and Sanders, R. (2001). Effect of thumb abduction and adduction on hydrodynamic characteristics of a model of the human hand. *Biomechanics Symposia*.

Terra, W., Sciacchitano, A., and Scarano, F. (2020). Cyclist reynolds number effects and drag crisis distribution. *Journal of Wind Engineering and Industrial Aerodynamics*, 200:104143.

Truijens, M. and Toussaint, H. (2005). Biomechanical aspects of peak performance in human swimming. *Animal Biology*, 55(1):17–40.

van den Berg, J., Bazuin, R., Jux, C., Sciacchitano, A., Westerweel, J., and van de Water, W. (2021). The effect of hand posture on swimming efficiency. *Experiments in Fluids*, 62(12).

van Houwelingen, J., Schreven, S., Smeets, J. B., Clercx, H. J., and Beek, P. J. (2017a). Effective propulsion in swimming: Grasping the hydrodynamics of hand and arm movements. *Journal of Applied Biomechanics*, 33(1):87–100.

van Houwelingen, J., Willemsen, D. H., Kunnen, R. P., van Heijst, G. F., Grift, E. J., Breugem, W. P., Delfos, R., Westerweel, J., Clercx, H. J., and van de Water, W. (2017b). The effect of finger spreading on drag of the hand in human swimming. *Journal of Biomechanics*, 63:67–73.

Vilas-Boas, J. P., Ramos, R. J., Fernandes, R. J., Silva, A. J., Rouboa, A. I., Machado, L., Barbosa, T. M., and Marinho, D. A. (2015). Hydrodynamic analysis of different finger positions in swimming: A computational fluid dynamics approach. *Journal of Applied Biomechanics*, 31(1):48–55.

Wei, T., Mark, R., and Hutchison, S. (2014). The fluid dynamics of competitive swimming. *Annual Review of Fluid Mechanics*, 46(1):547–565.

West, G. S. and Apelt, C. J. (1982). The effects of tunnel blockage and aspect ratio on the mean flow past a circular cylinder with reynolds numbers between 10^4 and 10^5. *J. Fluid Mechanics*, 114:361–377.

White, F. M. (2011). *Fluid Mechanics*. McGraw-Hill Education, London, seventh edition in si units edition.

Colophon

This document was typeset using LaTeX, using the KOMA-Script class `scrbook`. The main font is Palatino.